

Sub-solar electron temperatures in the lower Martian ionosphere

William K. Peterson¹, Laila Andersson², Robert E Ergun³, Edward Michael Benjamin Thiemann⁴, Marcin Dominik Pilinski⁴, Scott Alan Thaller¹, Christopher M Fowler⁵, David L. Mitchell⁶, Mehdi Benna⁷, Roger Yelle⁸, and Shane Wesley Stone⁸

¹University of Colorado Boulder

²Laboratory for Atmospheric and Space Physics (LASP)

³University of Colorado

⁴Laboratory for Atmospheric and Space Physics

⁵Space Sciences Laboratory

⁶University of California, Berkeley

⁷NASA Goddard Space Flight Center

⁸University of Arizona

November 24, 2022

Abstract

Martian sub-solar electron temperatures obtained below 250 km are examined using data obtained by instruments on the Mars Atmosphere Evolution Mission (MAVEN) during the three sub-solar deep dip campaigns and a one-dimensional fluid model. This analysis was done because of the uncertainty in MAVEN low electron temperature observations at low altitudes and the fact that the Level 2 temperatures reported from the MAVEN Langmuir Probe and Waves (LPW) instrument are more than 400 Kelvin above the neutral temperatures at the lowest altitudes sampled (~ 120 km). These electron temperatures are well above those expected before MAVEN was launched. We find that an empirical normalization parameter, neutral pressure divided by local electron heating rate, organized the electron temperature data and identified a similar altitude (~ 160 km) and time scale ($\sim 2,000$ s) for all three deep dips. We show that MAVEN data are not consistent with a plasma characterized by electrons in thermal equilibrium with the neutral population at 100 km. Because of the lack of data below 120 km and the uncertainties of the data and the cross sections used in the one dimensional fluid model above 120 km, we cannot use MAVEN observations to prove that the electron temperature converges to the neutral temperature below 100 km. However, the lack of our understanding of the electron temperature altitude profile below 120 km does not impact our understanding of the role of electron temperature in determining ion escape rates because ion escape is determined by electron temperatures above 180 km.

1 Sub-solar electron temperatures in the lower Martian ionosphere

2
3 W.K. Peterson¹, L. Andersson¹, R. Ergun¹, Ed Thiemann¹, Marcin Pilinski¹, S.
4 Thaller¹, C. Fowler², D. Mitchell², M. Benna³, R. Yelle⁴, and Shane Stone⁴.

5
6 ¹LASP, University Colorado Boulder

7 ²Space Science Laboratory, University of California, Berkeley

8 ³NASA Goddard Space Flight Center, Greenbelt, Md.

9 ⁴University of Arizona

10
11 Submitted to JGR Space Physics November, 2019

12 Abstract:

13 Martian sub-solar electron temperatures obtained below 250 km are examined using data
14 obtained by instruments on the Mars Atmosphere Evolution Mission (MAVEN) during the three
15 sub-solar deep dip campaigns and a one-dimensional fluid model. This analysis was done
16 because of the uncertainty in MAVEN low electron temperature observations at low altitudes
17 and the fact that the Level 2 temperatures reported from the MAVEN Langmuir Probe and
18 Waves (LPW) instrument are more than 400 Kelvin above the neutral temperatures at the
19 lowest altitudes sampled (~120 km). These electron temperatures are well above those
20 expected before MAVEN was launched. We find that an empirical normalization parameter,
21 neutral pressure divided by local electron heating rate, organized the electron temperature
22 data and identified a similar altitude (~160 km) and time scale (~2,000 s) for all three deep dips.
23 We show that MAVEN data are not consistent with a plasma characterized by electrons in
24 thermal equilibrium with the neutral population at 100 km. Because of the lack data below 120
25 km and the uncertainties of the data and the cross sections used in the one dimensional fluid
26 model above 120 km, we cannot use MAVEN observations to prove that the electron

27 temperature converges to the neutral temperature below 100 km. However, the lack of our
28 understanding the electron temperature altitude profile below 120 km does not impact our
29 understanding of the role of electron temperature in determining ion escape rates because ion
30 escape is determined by electron temperatures above 180 km.

31

32 Introduction:

33 The Mars Atmospheric Volatile Evolution (MAVEN, Jakosky et al., 2015) mission objective is
34 to obtain reliable observations of geophysical parameters that control or limit atmospheric
35 escape. Several processes such as the escape of energetic oxygen atoms depend strongly on the
36 plasma electron temperature (e.g. e.g. Fox and Hac, 2009; Andersson et al., 2010; Lillis et al.
37 2015; Ergun et al., 2016; Brecht et al., 2017). There have been many recent papers reporting
38 analysis of electron temperatures and their effect on the Martian thermosphere (e.g. Ergun et
39 al., 2015, 2016; Fowler et al., 2015; Mendillo et al., 2017; Flynn et al., 2017; Lillis et al., 2017;
40 Thiemann et al., 2018; Xu et al., 2018; and Peterson et al., 2018). These reports have focused
41 primarily on data acquired during normal operations, not during the nine so called deep dip
42 intervals, where the MAVEN periapsis was maintained below 140 km for several days.

43 Electron temperature data from the first sub-solar deep dip campaign have been analyzed
44 by Ergun et al., (2015) and Peterson et al., (2018). They reported Electron temperatures at 130
45 km less than 500 Kelvin but greater than the observed neutral temperature of ~100 Kelvin
46 (Stone et al., 2018). The 500 Kelvin value for electron temperature reported at 130 km is
47 significantly larger than was expected before MAVEN was launched (e.g. Fox, 1993, Shinagawa
48 and Cravens, 1989; Bougher et al., 2015; and Brecht et al., 2017).

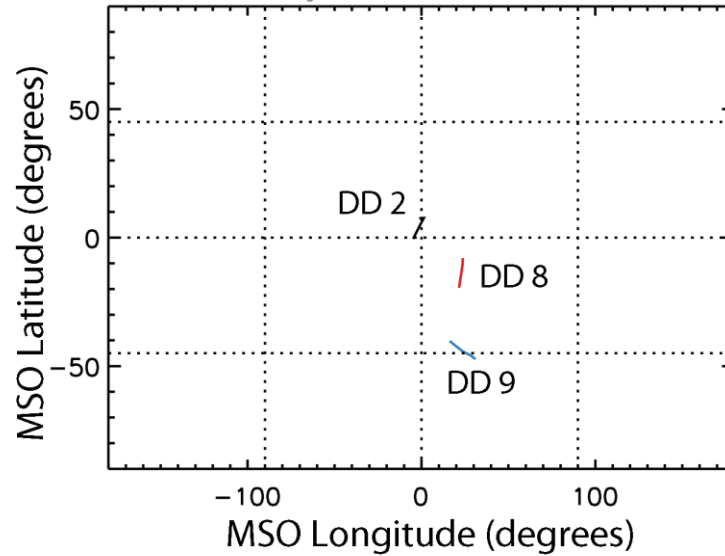
49 Ergun et al., (2015), and others have noted that the MAVEN electron temperatures
50 reported in the level 2 data product are known to be biased high at low temperatures (i.e. $T_E < 700$
51 Kelvin). The measurement uncertainties reported in the level 2 data product are empirically
52 derived as described in Fowler (2016). These empirical uncertainties are conservative estimates
53 that are quite large being on the order of ± 300 Kelvin for a 500 Kelvin electron temperature.

54 The purpose of this paper is to use MAVEN data acquired during the three MAVEN sub-
55 solar deep dip intervals and analysis to improve our understanding of the electron temperature
56 altitude profiles below 160 km.

57

58 Observations

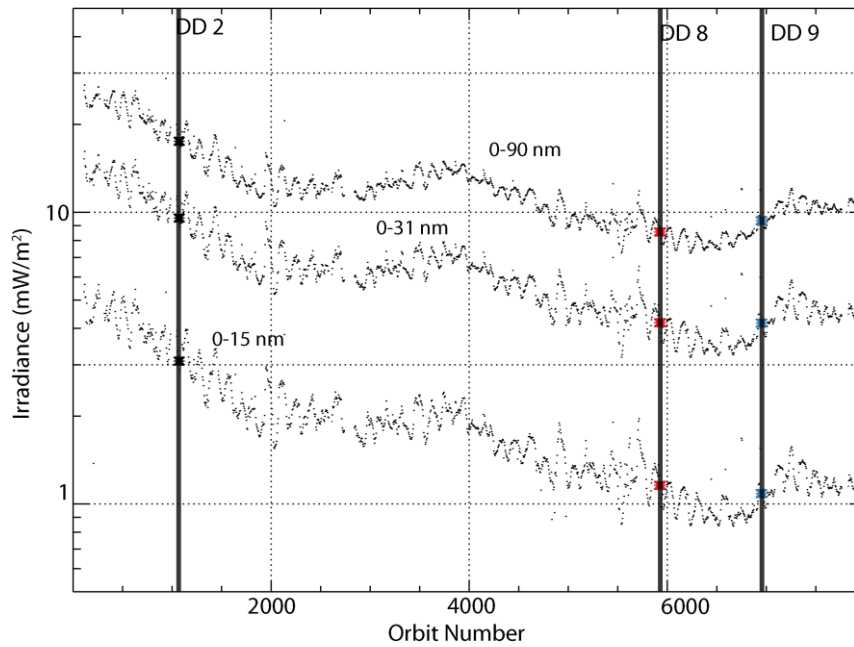
59 The MAVEN spacecraft performed nine deep dip campaigns, three of which sampled the
60 sub-solar region. During a deep dip campaign, the Martian thermosphere is sampled at altitudes
61 below 140 km for periods on the order of a week. The latitudes and longitudes sampled in deep
62 dip campaigns DD2, DD8, and DD9 in the Mars-centered Solar Orbital (MSO) coordinate
63 system are shown in Figure 1. DD2 (deep dip 2) was from April 17 to 22, 2015; DD8 was from
64 October 16 to 23, 2017; and DD9 was from April 24 to 30, 2018. Solar irradiance in three
65 selected wavelength bands from the MAVEN Extreme UltraViolet Monitor (EUVM, Epavier et
66 al., 2015) is presented in Figure 2. It shows that DD2 occurred early in the mission when solar
67 activity was higher than during DD8 and DD9.



68

69 Figure 1: Location in MSO latitude and longitude of the periapsis location of the inbound
 70 segments of MAVEN orbits from the three sub-solar deep dip campaigns. DD2 (deep dip 2) was
 71 from April 17 to 22, 2015; DD8 was from October 16 to 23, 2017; DD9 was from April 24 to 30,
 72 2018

73

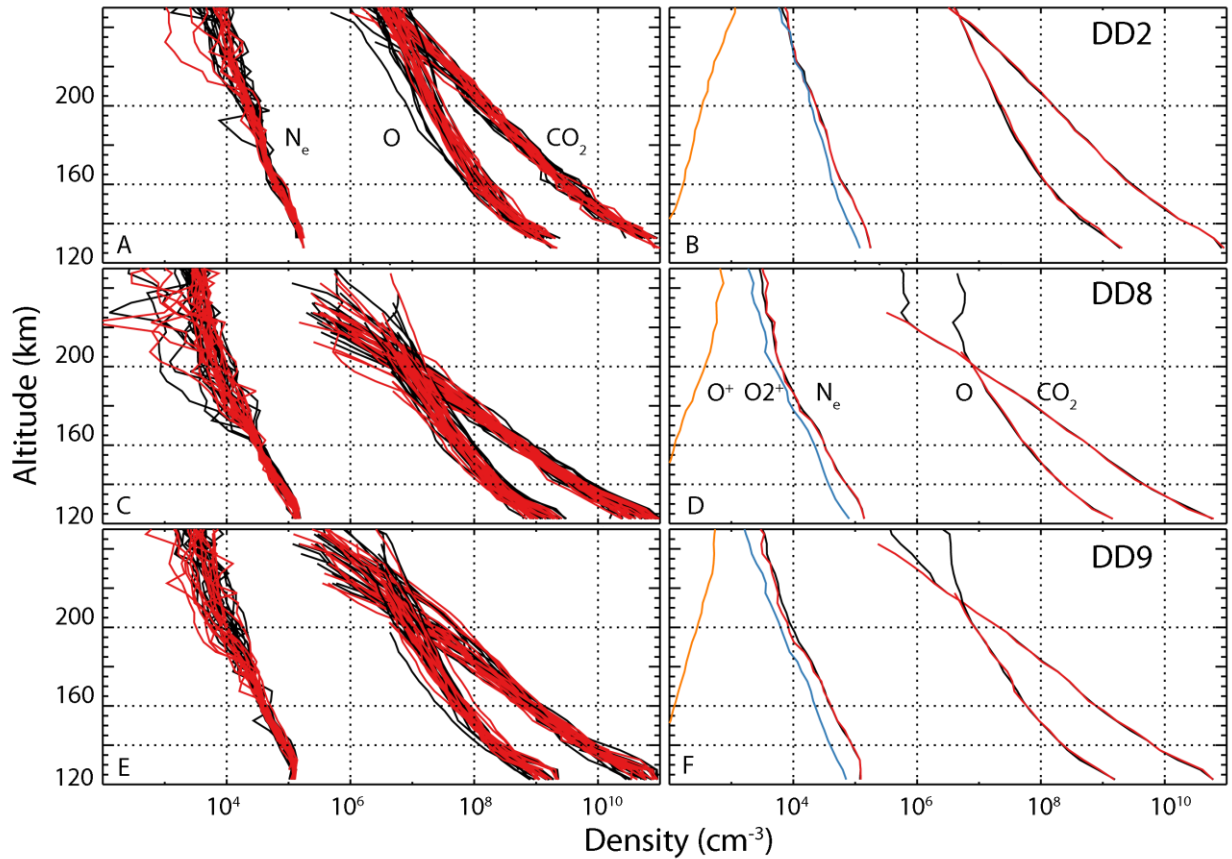


74

75 Figure 2. Solar EUV irradiance at Mars in the three indicated wavelength bands from the
 76 EUVM Level 3 daily spectral product. The orbit number range of the deep dip campaigns are
 77 indicated by the solid vertical lines.

78

79 Figure 3 presents the neutral, ion, and electron densities observed during the three deep
80 dip campaigns from the MAVEN Neutral Gas and Ion Mass Spectrometer (NGIMS, Mahaffy et
81 al., 2015) and Langmuir Probe and Waves (LPW, Andersson et al., 2015) instruments. Electron
82 and neutral data are presented for each orbit in the in the left column and as the median of all
83 observations in the right column. Median thermal Ion densities for the deep dip campaigns
84 from the NGIMS instrument are also shown in the right column. To eliminate effects of crustal
85 magnetic fields in their analysis, Peterson et al., (2018) considered only photoelectron data
86 from orbits where the magnetic field (Connerney et al., 2015) was nearly horizontal to the
87 Martian surface, i.e. for magnetic dip angles less than 30° . In Figure 3 electron and neutral
88 densities obtained for magnetic dip angles less than 30° are indicated by red lines and black for
89 dip angles larger than 30° . Below 200 km the divergence between the red and black electron
90 density data is minimal, indicating that magnetic field orientation does not significantly affect
91 ion and neutral densities. Careful examination of Figure 3 also shows that the sum of the O^+ and
92 O_2^+ densities is less than the reported electron density (N_E) for all three deep dip campaigns.
93 This difference is attributed to issues relating to the variable spacecraft potential, the limited
94 energy range of the NGIMS instrument, and other instrumental effects. The magnitude of the
95 difference in ion and electron density determinations is small compared to other uncertainties
96 in the calculation of cooling terms in the heat equation as discussed in Peterson et al., (2018).



97

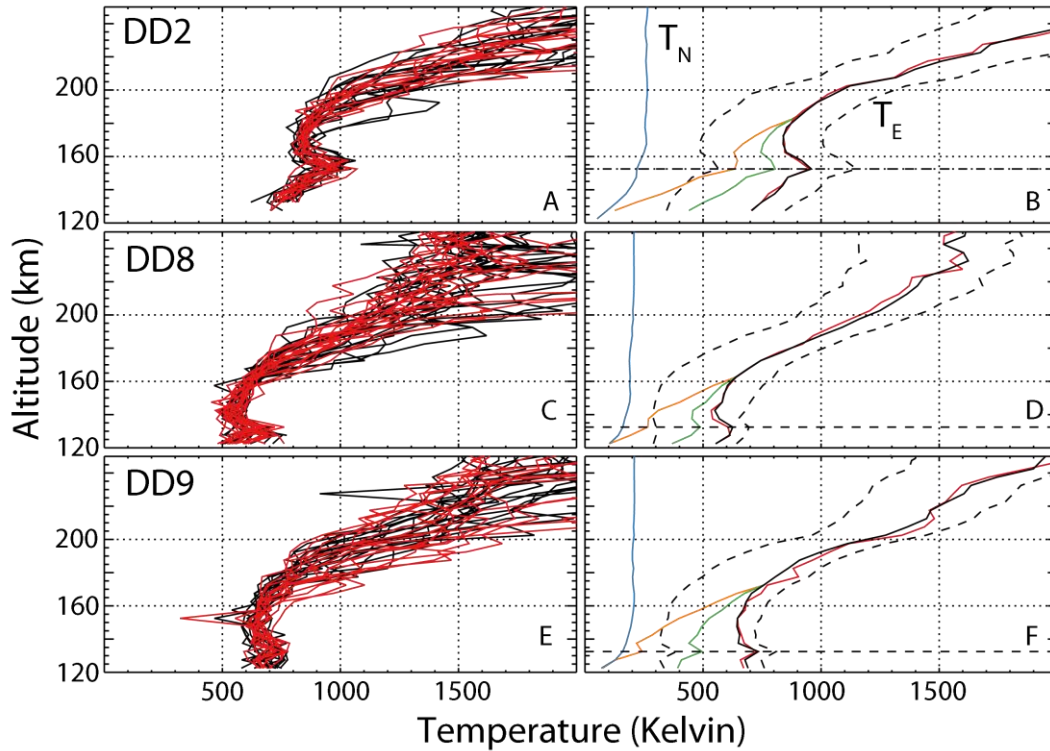
98 Figure 3: Electron, ion, and neutral densities from the three sub-solar deep dip campaigns
 99 for altitudes below 250 km. Panels A, C, and E show data for individual orbits; panels B, D, and F
 100 show the median values for all orbits in the deep dip campaign. In all panels electron, CO₂, and
 101 O densities are shown using both red and black colors. Red indicates orbits where the magnetic
 102 dip angle is less than 30° and black for orbits where it is not. In panels B, D, and E median
 103 densities of O⁺ and O₂⁺ are indicated by orange and blue lines respectively.

104

105 Observed electron temperatures (T_E) below 250 km from the three sub-solar deep dip
 106 campaigns are shown for each orbit in panels A, C, and E of Figure 4 and their median values in
 107 panels B, D, and F. Red indicates that the magnetic dip angle was less than 30°; black indicates
 108 that the magnetic dip angle was larger than 30°. Shown also in panels B, D, and F are neutral
 109 temperatures (T_N blue) reported by Stone et al, (2018), empirically derived upper and lower
 110 limits of the electron temperature (dashed lines, Fowler, 2016) and low altitude empirically

111 adjusted electron temperatures (discussed below and shown by green and orange lines). The
112 Andersson electron spike feature, an expected increase in electron temperatures at low sub-
113 solar altitudes (Andersson et al., 2019) is seen in the median values (panels B, D, and F) near
114 152 km in DD2 and 132 km in DD8 and DD9. No systematic difference in the electron
115 temperature profile as a function of dip angle is seen below 250 km, consistent with the results
116 of Sakai et al. (2019) obtained from a much larger data sample. Measured ion temperatures
117 from the Supra Thermal and Thermal Ion Composition instrument (STATIC, McFadden et al.,
118 2015) are not reported in Figure 4 because algorithms to account for all instrumental effects
119 encountered at thermal energies are not yet available (J. McFadden, private communication,
120 2019).

121



122

123 Figure 4: Electron temperatures from the level 2 data product obtained below 250 km from the
 124 three sub-solar deep dip campaigns are shown on a per orbit basis in panels A, C, and E. Their median
 125 values are shown in panels B, D, and F. As in Figure 3 red lines indicate data from orbits where the
 126 magnetic dip angle is less than 30° and black indicates where the dip angle is greater. Also shown in
 127 panels B, D, and F are neutral temperatures (blue) reported by Stone et al, (2018), empirically derived
 128 upper and lower limits of the electron temperature (dashed lines, Fowler et al., 2016) and low altitude
 129 empirically adjusted electron temperatures (green and orange lines, see text). The dashed horizontal
 130 lines in panels B, D, and F indicate the altitude of the Andersson T_e spike.

131

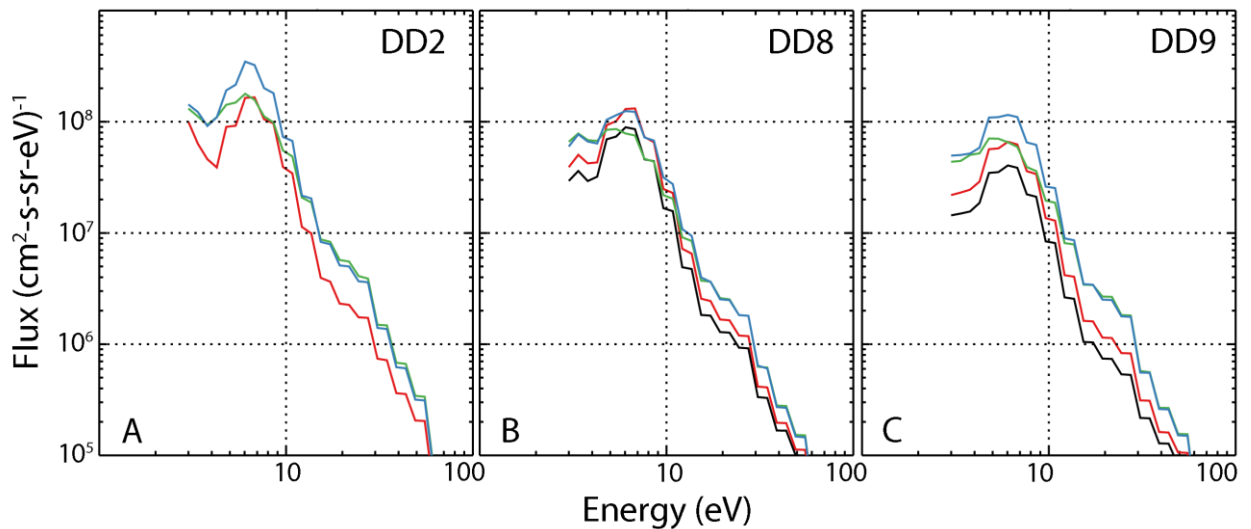
132 Below ~ 700 Kelvin, MAVEN electron temperatures reported in the level 2 LPW data
 133 product are known to be biased high (Ergun et al., 2015; Fowler, 2016, Peterson et al., 2018).
 134 The theoretical lower limit of the measurement is between 150 and 200 Kelvin. The upward
 135 bias in the value reported in the level 2 data likely arises from non-ideal behavior with regards
 136 to the operation of the Langmuir Probe in the highly variable plasma environment at Mars,
 137 including: variable sheath shape and size, ion wakes behind the probes, and non-uniform probe
 138 surfaces due to atomic oxygen contamination of the probe surfaces (Fowler 2016). The fitting
 139 process described in Fowler (2016) attempts to account for these non-ideal behaviors.

140 However, because LPW instrument is the first Langmuir Probe to be flown in such a variable
141 plasma environment, there are no other comparable Langmuir Probe data sets with which to
142 make comparisons and fully quantify these effects. The lower and upper temperature limits
143 reported for the L2 data are subsequently quite conservative (Fowler, 2016). A re-examination
144 of the fitting procedures used to obtain level 2 electron temperatures concluded that the
145 values reported below 700 Kelvin are at most biased 25% too high (Ergun, private
146 communication 2019). The empirically derived upper and lower limits of the electron
147 temperatures are shown as dashed lines in Figure 3. These conservative limits are more than
148 25% above and below the reported values.

149 A concept, rationale, and procedure to empirically adjust raw electron temperatures below
150 160 km obtained by the LPW instrument were presented in Peterson et al., (2018).
151 Extrapolations are made from altitudes and temperatures where, prior to the MAVEN launch, it
152 was generally assumed that electrons and neutrals were in thermal equilibrium at ~ 100 Kelvin
153 between 80 and 120 km (e.g. Gröller, Montmessin, Yelle, et al., 2018) to altitudes and
154 temperatures where the uncertainties in T_E observed by the LPW instrument are low compared
155 to the observed values. Two extrapolations of T_E are shown in Figure 4 panels B, D, and F for all
156 three deep dips. Orange lines show temperatures derived assuming electron-neutral thermal
157 equilibrium at 100 Kelvin at 120 km. Green lines show temperatures derived assuming electron-
158 neutral thermal equilibrium at 100 Kelvin at 80 km. The extrapolations retain the Andersson T_E
159 spike feature (Andersson et al., 2019).

160 Electron temperature is determined by a balance between heating and cooling rates of
161 electrons, ions, and neutrals. On the dayside, the primary source of energy for heating

162 electrons is the photoelectron population. Figure 5 presents the median photoelectron
 163 spectrum obtained from the MAVEN Solar Wind Electron Analyzer (SWEA) instrument (Mitchell
 164 et al., 2016) as a function of energy at altitudes indicated by the color code from each of the
 165 three dip campaigns. Photoelectron data are not obtained below 3 eV. The photoelectron data
 166 have been corrected for spacecraft potential and averaged over 5 km wide altitude bins. Data
 167 are shown centered at altitudes of 122 km (black), 127 km (red), 152 km (blue), and 182 km
 168 (green).



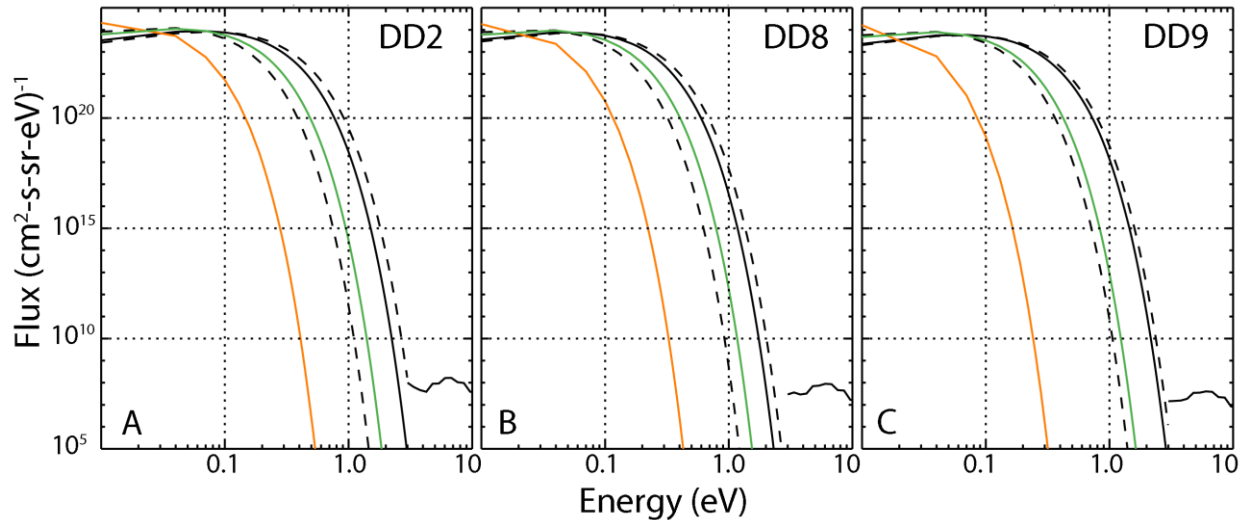
169 Figure 5: Median photoelectron fluxes as a function of energy from the three indicated sub-
 170 solar deep dip campaigns. The 5 km wide altitude bins over which the data are averaged are
 171 indicated by black (122 km), red (127 km), blue (152 km), and green (182 km). Note that during
 172 deep dip 2 (DD2), data were not obtained below 125 km.
 173

174
 175 Figure 6 presents the low energy portion of the photoelectron distributions seen in Figure 5
 176 and thermal electron fluxes calculated from a Boltzmann distribution using the observed
 177 electron density and temperatures shown in Figure 4 as a function of energy for the lowest
 178 altitude bin sampled during each of the three sub-solar deep dips. The solid black line above 3
 179 eV is a reproduction of photoelectron fluxes reported in Figure 5 at 127 km (DD2) and 122 km

180 (DD8 and DD9). The Boltzmann distributions shown were calculated from the lowest altitude
181 electron densities shown in Figure 3 and the five electron temperature values at the lowest
182 altitude sampled for the observed (level 2 data) in solid black lines, the upper and lower limits
183 reported in the level 2 data (dashed black lines), the extrapolation to 120 km (orange lines), and
184 the extrapolation to 80 km (green lines).

185 Dalgarno, McElroy, and Moffett (1963), and Rees (1989) have formulated empirical
186 relations to calculate local thermal electron heating rates from photoelectron energy spectra.
187 Both of these approaches involve an integral of the photoelectron flux above the energy, E_{CO} ,
188 where the thermal energy flux is equal to the photoelectron energy flux. As seen in Figure 6,
189 and confirmed by calculations not illustrated here, E_{CO} is below 3 eV in all cases. In particular,
190 the major contribution to the Rees and Dalgarno et al. integrals occurs for energies below 3 eV.
191 Thus, the photoelectron flux observations above 3 eV shown in Figures 5 and 6 do not directly
192 determine electron heating rates; the secondary electrons they produce both locally and
193 deeper in the atmosphere do. Peterson et al., (2018) developed an alternative method to
194 calculate the local electron heating rates which is used and discussed below.

195



196
 197 Figure 6: Thermal and photo electron energy spectra for the three deep dip campaigns at the
 198 lowest observed altitude. The solid black lines above 3 eV are reproduced from the lowest
 199 altitude photoelectron energy spectrum in Figure 5. The solid black line below 3 eV is a
 200 Boltzmann distribution calculated using the lowest altitude T_E and N_E values reported in the
 201 LPW level 2 data product. The dashed black lines are calculated using the upper and lower
 202 limits of T_E and N_E in the level 2 data product. The solid green and orange lines are calculated
 203 using the empirically adjusted temperatures shown in Figure 4.

204

205 Analysis and Discussion:

206

207 An alternative statement of the objective of this paper is to determine which, if any, of the

208 five low altitude temperature extrapolations shown in Figure 4 are consistent with both other

209 MAVEN observations and our current understanding of electron thermalization processes.

210 Because there are no observations of the thermal/photoelectron energy spectrum near E_{CO} , we

211 must rely on a fully kinetic model of the thermal and photoelectron plasma, or the fluid model

212 developed over 40 years ago and described by, among many others, Schunk and Nagy (2009),

213 Mata et al., (2014), and Peterson et al., (2018). Here we use the one-dimensional fluid model

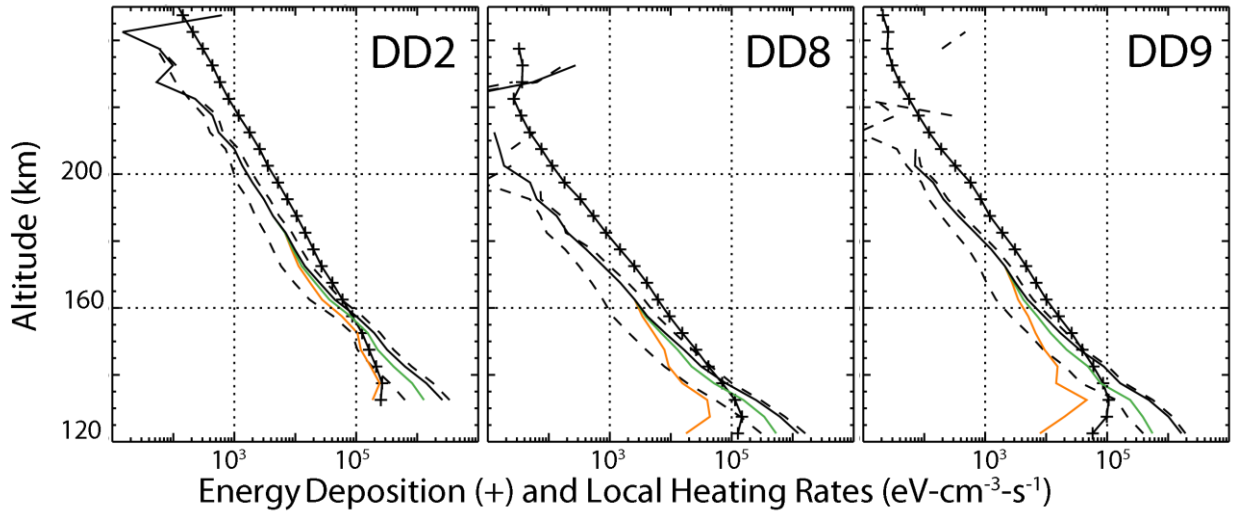
214 and cross sections presented by Mata et al., (2014) and Peterson et al., (2018). The method

215 does not use a photoelectron transport code. It uses the concept of electron heating efficiency

216 to account for the transfer of energy produced by photoionization to local electrons. Local
217 thermal electron heating and cooling rates for each of the electron temperature profiles are
218 calculated as described below.

219 Figure 7 presents EUV energy deposition and electron heating rate profiles for the three
220 sub-solar deep dip campaigns. The black line with + symbols in Figure 7 shows energy
221 deposition associated with photoionization calculated from the neutral densities shown in
222 Figure 3 and a Solar EUV spectrum constrained by MAVEN observations (Thiemann et al., 2017).
223 The other lines in Figure 7 show the sum of thermal electron cooling rates, convection,
224 advection, and expansion rates calculated using MAVEN data shown in Figures 3 and 4 and the
225 five low altitude temperature extrapolations shown in Figure 4. Note that these calculations
226 and those by Peterson et al., (2018) use the Campbell et al, (2008) inelastic e-CO₂ cross section
227 instead of the Dalgarno (1969) cross sections given as equation A12 by Matta et al., (2014). This
228 approach includes electron – ion and electron – neutral collisions and approximates the ion
229 temperature (T_i) as the average of T_E and T_N .

230 Assuming thermal equilibrium, the electron heating rate equals the sum of the cooling,
231 convection, advection, and expansion rates (e.g. Mata et al., 2004, Peterson et al., 2018). Above
232 ~ 160 km electron energy deposition is greater than the local electron heating rates. This arises
233 because energetic photoelectrons produced above 160 km transport significant energy to lower
234 altitudes.



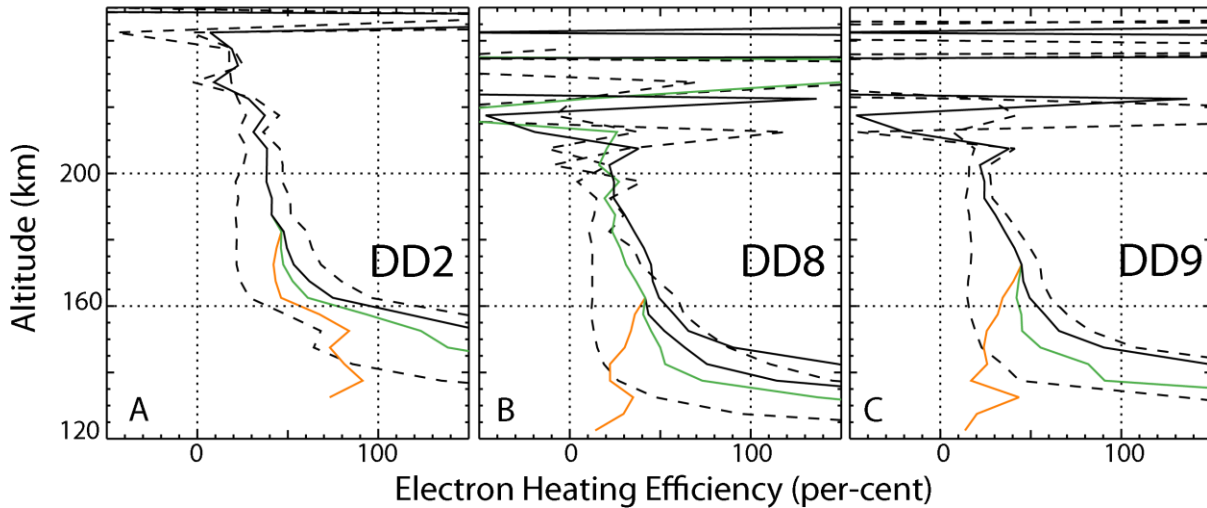
235
 236 Figure 7: Energy Deposition (black lines with + symbols) and the sum of cooling, advection,
 237 conduction, expansion, conduction and local electron heating rates calculated using the one-
 238 dimensional model described by Mata et al., (2014) and Peterson et al., (2018). Sums are shown
 239 for the 5 temperature altitude profiles shown in Figure 4. The solid black line was calculated
 240 using the T_E and N_E values in the LPW level 2 data product. The dashed black lines are calculated
 241 using the upper and lower limits of T_E and N_E in the level 2 data product. The solid green and
 242 orange lines are calculated using the empirically adjusted temperatures shown in Figure 4. Note
 243 that under the assumption of local thermal equilibrium the sum of the cooling, advection,
 244 conduction, expansion, conduction terms is equal to the local thermal electron heating rate.

245
 246 Peterson et al., (2018) defined electron heating efficiency as ratio of the local electron
 247 heating rates to the energy deposition rate. This approach does not require a photoelectron
 248 transport code or the calculation of ionization efficiencies (e.g. Cui et al., 2018). Figure 8 shows
 249 the inferred electron heating efficiency as a function of altitude for the three deep dip
 250 campaigns and the five low altitude temperature extrapolations under consideration. Electron
 251 heating efficiencies above 100% indicate that energetic photoelectrons produced at higher
 252 altitudes are transporting and depositing their energy at lower altitudes. Above ~ 200 km,
 253 heating efficiencies are not well organized by altitude and are sometimes negative, especially
 254 for deep dips 8 and 9. Above ~ 200 km the heat conduction term in the heat equation becomes
 255 significant and variable (Peterson et al., 2018). Other contributions to the variability above ~ 200

256 km come from temporal and spatial variations in the inputs to the heat equation not captured
257 in the deep dip average values used in the calculations of cooling, advection, conduction, and
258 expansion, rates. See, for example, Fowler et al., (2018a, b). Figure 8 demonstrates that
259 electron heating efficiency below ~ 200 km depends strongly on the electron temperature.

260 Four of the five electron heating efficiency altitude profiles exceed 100% between 130 and
261 160 km; one of them (the temperature extrapolation to 100 Kelvin at 120 km, indicated by
262 orange lines) does not. Errors in the calculating the heating efficiency are large because the
263 calculation involves the sum of many terms as described in Peterson et al., (2018). A similar
264 error analysis shows that the reported heating efficiencies greater and less than 100% in Figure
265 8 are statistically significant.

266 An altitude profile of heating efficiency that does not exceed 100% above the altitude of
267 peak EUV absorption (~ 120 km) is not physically realistic because it implies that there is no
268 region in the Martian ionosphere where transport of energetic photoelectrons from higher
269 altitudes is significant. We conclude that the electron temperature profile extrapolated to 100
270 Kelvin at 120 km is not consistent with MAVEN data and the one-dimensional model we used.



271

272 Figure 8: Inferred electron heating efficiencies as a function of altitude for the three deep
 273 dip campaigns and the five low altitude temperature extrapolations under consideration. The
 274 solid black line was calculated using the T_E and N_E values in the LPW level 2 data product. The
 275 dashed black lines are calculated using the upper and lower limits of T_E and N_E in the level 2
 276 data product. The solid green and orange lines are calculated using the empirically adjusted
 277 temperatures shown in Figure 4. The profile using the lowest temperatures indicated by solid
 278 orange lines was found to be non-physical (see text).

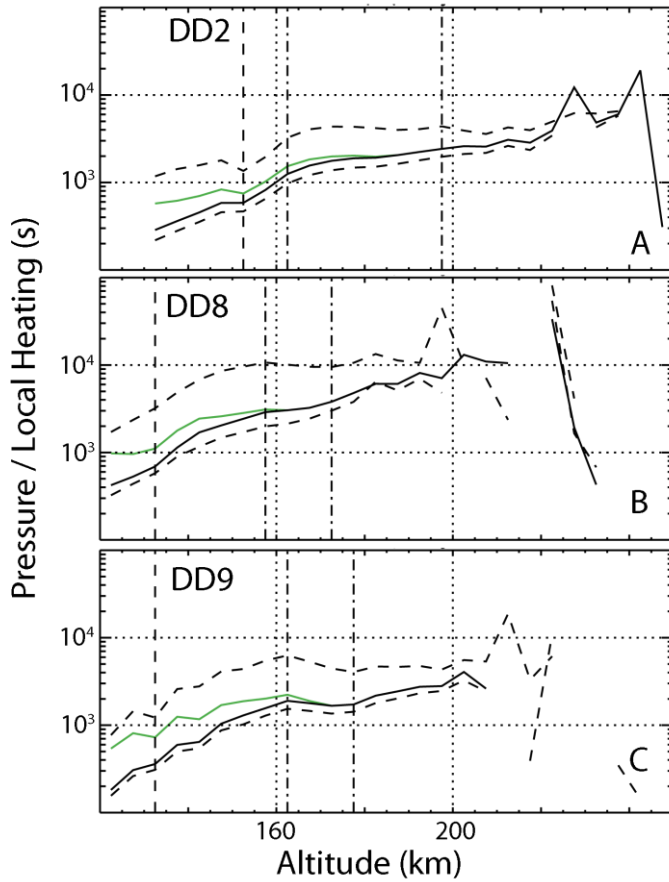
279

280 Electron temperature altitude profiles vary systematically with EUV irradiance and Martian
 281 season. Data exploration not illustrated here demonstrated that plotting T_E as a function of
 282 neutral pressure divided by the local electron heating rate (P/LEH) reduced some of the
 283 systematic variability with season and EUV irradiance. Here neutral pressure is the product of
 284 neutral density (CO_2 and O from Figure 3) and neutral temperature (Figure 4). Local electron
 285 heating is calculated as the product of EUV energy deposition (Figure 7) and electron heating
 286 efficiency (Figure 8). We note that the units of P/LEH are seconds.

287 Figure 9 presents P/LEH as a function of altitude for each of the sub-solar deep dip
 288 campaigns calculated using four electron temperature profiles: The LPW Level 2 values (solid
 289 black lines) and empirical upper and lower limits (dotted black lines) as well as the empirical

290 temperature profile that reaches 100 K at 80 km (solid green lines). For DD2 MAVEN data were
291 not acquired at the lowest altitudes and therefor the heating rate calculations are not available.
292 The systematic errors in calculating heating efficiency discussed above preclude using the P/LEH
293 parameter above ~ 200 km in the sub-solar region. Shown also in Figure 9 are the altitudes of
294 the Andersson T_E spike (vertical dashed lines), and the altitudes where the optical depth of EUV
295 irradiance is 1 and 3 (vertical dashed dotted lines). Optical depth 1 and 3 correspond to
296 altitudes where 63% and 95% of the incident EUV irradiance is absorbed respectively. Optical
297 depth of 3 occurs near 160 km for all cases, but optical depth of 1 varies over a wide altitude
298 range in the three deep dip campaigns investigated.

299 The shape of the P/LEH vs. altitude plots has two regions of different slope separated by a
300 knee located near the altitude where the optical depth is approximately three. Below this
301 altitude energetic photoelectron production is less important. The knee occurs for P/LEH values
302 between 1000 and 2000 seconds or a frequency of $\sim 10^{-3}$ seconds. These times / frequencies are
303 not characteristic of any of the local plasma parameters, being an order of magnitude larger
304 than the typical O_2^+ ion gyro period. This time scale is more characteristic of planetary scale
305 thermospheric motions.



306

307 Figure 9. Altitude vs neutral pressure over local heating rates (P/LEH). Data are shown for 4
 308 T_E profiles. Solid black present the LPW Level 2 values. The black dashed lines present the
 309 empirical upper and lower limits from the LPW Level 2 data product. The green lines present
 310 empirical T_E extrapolations to 100 Kelvin at 80 km. The altitudes of the Andersson T_E spikes are
 311 shown by vertical dashed lines. The altitudes where the optical depth of EUV irradiance is 1 and
 312 3 are shown by vertical dashed dotted lines. See text.

313

314

315 Figure 10 presents Electron temperature as a function of altitude (left, panels A, C and E)

316 and electron temperature as a function of the ratio of neutral pressure to local electron heating

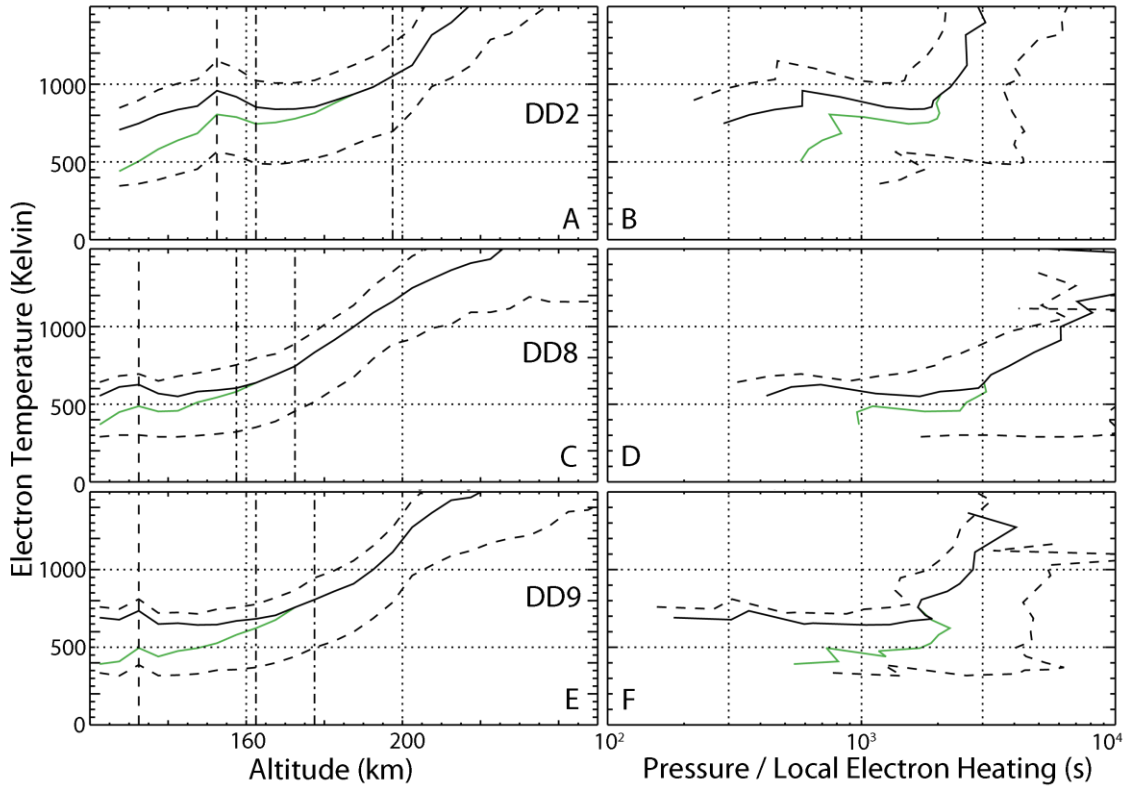
317 rate (P/LEH) right, panels B, D, and F). The color code and line styles follows those in Figure 9. In

318 panels A, C, E dashed vertical lines are shown at the altitude of the observed Andersson T_E

319 spike. The dash dot vertical lines in panels A, C, and E are shown where the EUV optical depth is

320 1 and 3. The data in panels B, D, and F show that the variations in T_E as a function of season and

321 solar cycle follow more similar patterns when compared to the altitude distributions seen in
 322 panels A, C, and E.



323
 324
 325 Figure 10: Electron temperature as a function of altitude (left, panels A, C and E) and electron
 326 temperature as a function of the ratio of neutral pressure to local electron heating rate (P/LEH ,
 327 right, panels B, D, and F). The color code and line styles follows that in Figure 9. Values
 328 calculated using the reported LPW level 2 electron temperature values are shown as solid black
 329 lines. Values calculated using the empirical upper and lower electron temperature values are
 330 shown as dashed black lines. Values calculated using the extrapolation to 100 Kelvin at 80 km
 331 are shown as green lines. In panels A, C, E dashed vertical lines are shown at the altitude of the
 332 observed Andersson T_E spike. The dash dot vertical lines in panels A, C, and E are shown where
 333 the EUV optical depth is 1 and 3 i.e. 63% and 95% of the incident solar EUV irradiances has been
 334 absorbed above this altitude. See text.

335
 336 The four different temperature altitude profiles in panels A, C, and E of Figure 10 differ in
 337 slope. The reported Level 2 temperature profiles and their empirical upper and lower limits
 338 (solid and dashed black lines) have a smaller slope below the altitude where the optical depth is
 339 about 3. The data in panels B, D, and F show that T_E data are essentially independent of the

340 P/LEH parameter below $2-3 \times 10^3$ seconds. Above $2-3 \times 10^3$ seconds the T_E vs. P/LEH data have
341 approximately constant slopes with different values of the slope for each deep dip. The knee in
342 the P/LEH vs. altitude plot in Figure 9 near the altitude with an optical depth of three is located
343 below $2-3 \times 10^3$ s in the T_E vs. P/LEH display.

344 The data presented in panels B, C, and F raise two questions that are related to the relative
345 importance of electron thermalization processes as a function of altitude. 1) What is the
346 significance, if any, of T_E being relatively independent of P/LEH below $\sim 2-3 \times 10^3$ seconds? 2)
347 What is the significance, if any, of the value $2-3 \times 10^3$ seconds?

348 The answer to question 2 is uncertain. $2-3 \times 10^3$ seconds and its associated frequency are
349 not characteristic of any local plasma parameters but rather are characteristic of planetary
350 scale thermospheric motions. It is difficult to interpret this answer in terms of Martian
351 thermospheric properties however. Since ion and/or neutral motion on this time scale is
352 associated with planetary scale thermospheric motions, it is not clear how this time scale
353 comes from our calculations using in-situ observations and a one-dimensional (vertical) model
354 with the assumptions of local thermal equilibrium. Transport of energy associated with ions and
355 neutrals is not considered in our formulation. Transport of electron energy is included in our
356 calculations only as a function of altitude.

357 Regarding question 1: What is implied by the fact that T_E is independent of a parameter,
358 such as pressure divided by local heating (P/LEH) below ~ 200 km and above the 120 km lower
359 limit of our observations (and for values of P/LEH below $2-3 \times 10^3$ s)? The answer is ambiguous.
360 It is commonly assumed that electrons equilibrate to the neutral temperature at some low
361 altitude. The observed neutral temperatures shown in Figure 4 are well below the

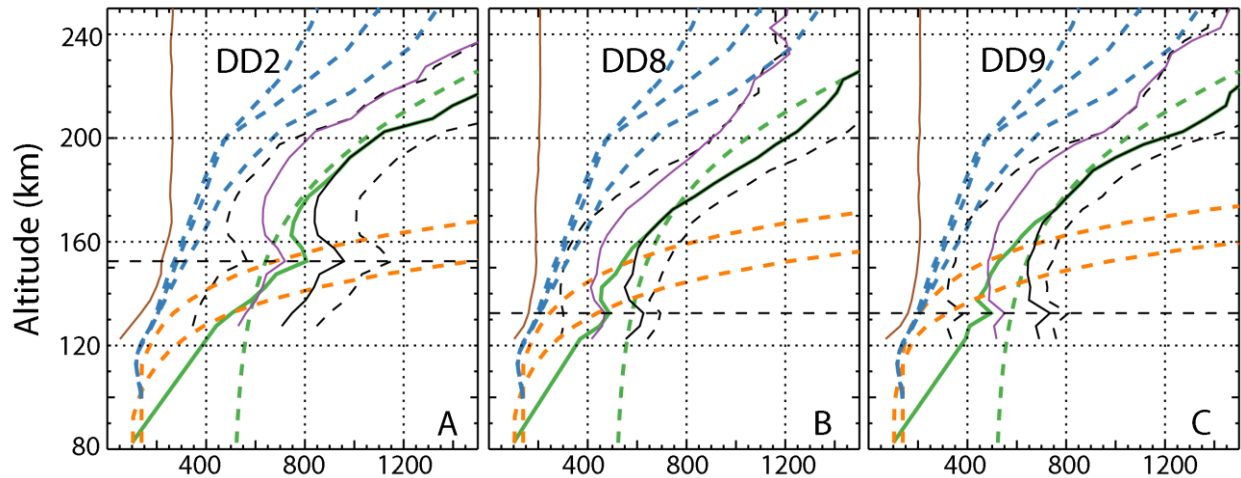
362 approximately constant electron temperature for P/LEH at values less than $2-3 \times 10^3$ seconds
363 for all four temperature profiles considered in Figure 10. These facts imply either that T_E falls to
364 the value of T_N (~ 100 Kelvin) well below 120 km (200 seconds in units P/LEH) or our one-
365 dimensional code which uses some poorly determined cross sections and an empirical ion
366 temperature profile does not adequately account for energy transfer between and among ions,
367 neutrals, and electrons at the low temperatures encountered at low altitudes on Mars.

368 Finally, we compare the electron temperature profiles discussed above with recent
369 predictions and/or models of Martian electron temperatures at altitudes below 160 km in
370 Figure 11. As in Figures 9 and 10, solid black lines indicate the observed temperature reported
371 in the MAVEN/LPW level 2 archived data product. The dashed black lines are the empirical
372 upper and lower temperatures as described by Fowler (2018a) and reported in the level 2 data
373 product. The solid purple line is drawn at 75% of the level 2 T_E . As noted above, a re-analysis of
374 selected data lead to the conclusion that the level 2 T_E upward bias is less than 25%. Below \sim
375 200 km the uncertainty in the reported T_E is significantly less the empirical estimate reported in
376 the level 2 data product and indicated by dashed black lines. The solid green line presents the
377 empirical low altitude temperature extrapolation to 100 Kelvin at 80 km presented in Figure 4.
378 Recent temperature profiles from Ergun et al., (2015, dashed green lines), Withers et al., (2014,
379 dashed orange lines), and Sakai et al., (2016, dashed blue lines) are also shown in Figure 11. The
380 Ergun et al., (2015) fit to the deep dip 2 data is consistent within the empirical observational
381 uncertainties of all of MAVEN/LPW temperatures for all altitudes in all three deep dip intervals.
382 The electron temperatures profiles reported Sakai et al., (2016) extended to 100 km and were
383 calculated for orbits before deep dip 2 and are therefore most comparable to the data obtained

384 in deep dip 2. The Sakai electron temperature calculations are consistently below those
385 reported above from all other sources at all altitudes.

386 The electron temperatures derived following the analysis of Withers et al., (2014, dashed
387 orange lines in Figure 11) used the observational solar zenith angles, and three parameters, T_N ,
388 Z_{pp} and H_o . The dashed orange curves with the highest temperature at 80 km uses $Z_{pp}=120$
389 km, H_o 10 km and a neutral temperature (T_N) of 100 Kelvin. The dashed orange curve with the
390 lowest temperature at 80 km uses $Z_{pp}=100$ km, $H_o=10$ km and a neutral temperature of 75
391 Kelvin. Both temperature profiles derived using the Withers' relations are consistently below
392 MAVEN / LPW values above about 150 km. The Withers et al., analysis suggests a stronger
393 dependence of electron temperature with altitude above ~ 120 km than those reported in the
394 LPW level 2 data products (black solid and dashed lines), Sakai et al., (2016, blue dashed lines),
395 and the empirical extrapolation to 100 Kelvin at 80 km (solid green lines).

396



397

398 Figure 11. Electron temperature comparisons for the three sub-solar deep intervals. Solid
 399 black lines are the MAVEN/LPW T_E data from the level 2 data product. Black dashed lines
 400 present the empirical upper and lower limits of MAVEN/LPW T_E given in the level 2 data
 401 product. The solid purple line is 75% of the level 2 electron temperature (see text). The solid
 402 green line is the empirical low altitude/temperature extrapolation to 100 Kelvin at 80 km
 403 reproduced from Figure 4. The solid brown line are neutral temperatures (Stone et al., 2018)
 404 reproduced from Figure 4. The dashed blue lines are from Sakai et al., (2016). The dashed green
 405 lines reproduce the best fit reported by Ergun et al., (2015). The dashed orange lines were
 406 calculated using relations reported by Withers et al., (2014) and the parameters noted in the
 407 text. Dashed horizontal lines are presented at the altitude of the Andersson T_E spike.

408

409

Below ~ 120 km the 4 temperature profiles shown in Figure 11 fall into two classes. The
 410 Ergun et al., (2015, dashed green lines) fit to deep dip 2 data that does not converge to the
 411 neutral temperature at lowest altitudes and all others. The other profiles all converge to a
 412 neutral temperature which is not measured but is an input to the calculation determining the
 413 profile. The Sakai et al., (2016, blue dashed lines) and Withers et al. (2014, orange dashed lines)
 414 fits are derived from approximations to the standard fluid model described by Schunk and Nagy
 415 (2009), with the neutral temperature used as an input parameter to calculating electron
 416 temperature. The empirical fit to the low altitude data indicated by the solid green line
 417 (Peterson et al., 2018) assumes an altitude and temperature where electrons and ions
 418 equilibrate. We note that the low altitude ~ 100 Kelvin neutral temperature observed by Stone

419 et al., (2018), and used by Sakai, Withers, and Peterson is at the low end of the neutral dayside
420 temperatures reported from MAVEN EUVM observations by Gröller et al., (2018). The low
421 altitude limit of electron temperature from the Ergun fit is well above the upper end of neutral
422 dayside temperatures reported by Gröller et al., (2018).

423

424 Conclusions:

425

426 Electron temperatures and their empirical upper and lower limits reported in the
427 MAVEN/LPW Level 2 data products from the three sub-solar deep dip campaigns of the MAVEN
428 mission have been examined. The analysis was based on a one-dimensional formulation of the
429 fluid model commonly known as the heat equation using data obtained from MAVEN
430 instruments following the procedures described here and by Peterson et al., (2018). The
431 method does not use a photoelectron transport code. It uses the concept of electron heating
432 efficiency to account for the transfer of energy produced by photoionization at all altitudes to
433 local electron heating. This approach requires knowledge of the local ion temperature, T_i . In
434 this analysis T_i is assumed to be the average of T_E and T_N .

435 The electron temperature altitude profiles are consistent with previous results reported
436 from the MAVEN/LPW instrument during normal, i.e. non deep dip operations (e.g. Fowler et
437 al., 2018a, 2018b, and Peterson et al. 2018). The electron temperatures below ~200 km were
438 also shown to be independent of magnetic field orientation, consistent with the results of Sakai
439 et al., (2019)

440 The MAVEN/LPW electron temperatures reported in L2 data products are thought to be
441 biased high. The difference between the empirical upper and lower limits originally reported in

442 the level 2 data product, are quite large (300 to 500 Kelvin) as shown in Figure 11. The re-
443 analysis of MAVEN/LPW data summarized above for electron temperatures less than 750 Kelvin
444 suggests that the upward bias in the Level 2 values is, at most, 25%, which is considerably
445 smaller than the empirical upper and lower limits of electron temperature included in the Level
446 2 data product.

447 The focus of the analysis presented above is on altitudes below 160 km. This analysis is
448 necessary because of the uncertainty in low electron temperature observations at low altitudes
449 and the fact that the Level 2 temperatures reported are more than 400 Kelvin above the neutral
450 temperatures at the lowest altitudes sampled (~120 km) which are well above those expected
451 before MAVEN was launched (e.g. Fox, 1993, Shinagawa and Cravens, 1989; Bougher et al.,
452 2015; and Brecht et al., 2017).

453 Following Peterson et al., (2018) we introduced empirical electron temperature altitude
454 profiles for the three deep dip campaigns that: 1) Reached 100 Kelvin at 120 and 80 km
455 respectively; 2) Merged with the electron temperature in the Level 2 data product above ~160
456 km; and 3) Retained the Andersson T_E spike below 160 km (Andersson et al., 2019). We
457 demonstrated that the lowest temperature profile, the one that reaches 100 Kelvin at 120 km,
458 when input to the heat equation, leads to the un-physical result that there is no region in the
459 Martian ionosphere where transport of energetic photoelectrons from higher altitudes is
460 significant.

461 To be better able to compare temperature profiles consistent with the heat equation
462 obtained during different Martian seasons and solar activity we examined electron temperature
463 as a function of pressure over local heating rates (P/LEH) in Figures 9 and 10. We found that

464 this display identified two temperature regimes in the observed data shown in solid black lines:
465 Those above and below values of P/LEH of 2000-3000 seconds. Above this value electron
466 temperature linearly increased with values of P/LEH. Below 2000 to 3000 seconds the electron
467 temperature profiles were relatively independent of the P/LEH parameter in the range
468 investigated. This is a time scale associated with planetary scale thermospheric motions. We
469 could not identify a correlation of this time scale with any specific process.

470 An examination of recent model and data analysis of electron temperature below the 120
471 km MAVEN observational limit identified two classes:

472 1) Where the electron temperature was forced to converge on a neutral temperature that
473 was empirically selected, not predicted. These include two based on the heat equation (Withers
474 et al., 2014, and Sakai et al., 2016) and the empirical fit (shown as green lines in Figure 11). The
475 neutral temperatures used were all at the low end of the range of neutral temperatures
476 reported by Gröller et al. (2018);

477 2) Those not forced to converge on a neutral temperature. The Ergun et al., (2015) fit to
478 observed deep dip 2 electron temperatures was made independent of any assumption on the
479 neutral temperature. The low altitude limit of electron temperature from the Ergun fit is well
480 above the upper end of neutral dayside temperatures derived from MAVEN optical
481 observations and reported by Gröller et al., (2018).

482 Above 120 km, the analysis shows that the Sakai et al. (2016) temperature profiles are too
483 low and inconsistent with the heat equation when MAVEN observations are used as input
484 parameters. The Withers et al., (2014) model of low altitude electron temperatures is derived
485 from three ad-hoc parameters (height, scale height, and neutral temperature). We found that,

486 between 120 and 160 km, there is consistency between the Withers' temperature profile using
487 carefully selected input parameters and MAVEN observations. Above ~160 km, the Withers'
488 predictions are all too high. The empirical fit to the data that converges to a 100 Kelvin neutral
489 temperature at 80 km introduced here is also consistent with MAVEN observations. The Ergun
490 et al., (2015) fit to DD2 data is consistent MAVEN observations for all three deep dip intervals
491 considered.

492 Because of the lack of low altitude data and the uncertainties of the data and one
493 dimensional one electron temperature fluid model above 120 km, we *cannot* use MAVEN
494 observations to prove that the electron temperature converges to the neutral temperature
495 below 100 km. The common wisdom is that T_E converges to T_N at some altitude, now below
496 100 km. If T_E does not converge to T_N , then a possible reason is that our one-dimensional code
497 which uses an empirical ion temperature profile and some poorly determined cross sections
498 does not adequately account for energy transfer between ions, neutrals, and electrons at the
499 low temperatures encountered at low altitudes on Mars. Perhaps a particle in cell code which
500 does not use assumed electron and ion temperature profiles will be able to resolve this
501 question.

502 The lack of our understanding the electron temperature altitude profile below 120 km,
503 however, does not impact our understanding of the role of electron temperature in
504 determining ion escape rates because ion escape is determined above ~180 km (Ergun et al.,
505 2016; Brecht et al., 2017).

506

507 Acknowledgements:

508

509 We thank the many 100's of people who made the MAVEN project successful. This work

510 was sponsored by NASA through the Mars Exploration Program. MAVEN data are available on

511 NASA's Planetary Data System.

512 References:

513

514

515 Andersson, L., R. E. Ergun, and A. I. F. Stewart (2010), The combined atmospheric
516 photochemistry and ion tracing code: Reproducing the Viking lander results and initial
517 outflow results, *Icarus*, 206(1), 120–129.

518 Andersson, L., R. E. Ergun, G. T. Delory, A. Eriksson, J. Westfall, H. Reed, J. McCauly, D.
519 Summers, and D. Meyers (2015), The Langmuir probe and waves (LPW) instrument for
520 MAVEN, *Space Sci. Rev.*, doi:10.1007/s11214-015-0194-3.

521 Andersson, L., C.M. Fowler, A Nagy, R. Yelle, T. Cravens, S. Bougher, A.G. Burns (2016),
522 Unexpected Diurnal Variations in Electron Temperature in the Mars Ionosphere, 2016 AGU
523 Fall Meeting Paper SA51C

524 <https://agu.confex.com/agu/fm16/meetingapp.cgi/Paper/170321>

525 Bougher, S. W., Pawlowski, D., Bell, J. M., Nelli, S., McDunn, T., Murphy, J. R., Chizek, M.,
526 and Ridley, A. (2015), Mars Global Ionosphere-Thermosphere Model: Solar cycle, seasonal,
527 and diurnal variations of the Mars upper atmosphere. *J. Geophys. Res. Planets*, 120, 311–
528 342. doi: [10.1002/2014JE004715](https://doi.org/10.1002/2014JE004715).

529 Brecht, S. H., Ledvina, S. A., and Jakosky, B. M. (2017), The role of the electron temperature
530 ion loss from Mars, *J. Geophys. Res. Space Physics*, 122, 8375– 8390,
531 doi:[10.1002/2016JA023510](https://doi.org/10.1002/2016JA023510).

532 Campbell, L., M. J. Brunger, and T. N. Rescigno (2008), Carbon dioxide electron cooling rates in
533 the atmospheres of Mars and Venus, *J. Geophys. Res.*, 113, E08008,
534 doi:10.1029/2008JE003099.

535 Connerney, J. E. P., et al., The MAVEN magnetic field investigation. *Space Sci. Rev.*
536 10.1007/s11214-015-0169-4 (2015). doi: 10.1007/s11214-015-0169-4

537 Cui, J., X.-S. Wu, S.-S. Xu, et al. (2018), Ionization efficiency in the dayside Martian upper
538 atmosphere, *Ap. J. Lett.*, 857:L18, <https://doi.org/10.3847/2041-8213/aabcc6>

539 Dalgarno, A, M.B. McElroy, and R.J. Moffett (1963), Electron temperatures in the ionosphere,
540 *Planet. Space Sci.*, 11, 463-484, doi: [10.1016/0032-0633\(63\)90071-0](https://doi.org/10.1016/0032-0633(63)90071-0)

541 Dalgarno, A., 1969. Inelastic collisions at low energies. *Can. J. Chem.* 47, 1723–1729.

542 Eparvier, F. G., P. C. Chamberlin, T. N. Woods, and E. M. B. Thiemann (2015), The solar extreme
543 ultraviolet monitor for MAVEN, *Space Sci. Rev.*, doi:10.1007/s11214-015-0195-2.

544 Ergun, R. E., M. W. Morooka, L. A. Andersson, C. M. Fowler, G. T. Delory, D. J. Andrews, A. I.

545 Eriksson, T. McEnulty, and B. M. Jakosky (2015), Dayside electron temperature and density

546 profiles at Mars: First results from the MAVEN Langmuir probe and waves instrument,
547 *Geophys. Res. Lett.*, 42, 8846–8853, doi:10.1002/2015GL065280.

548 Ergun, R. E., et al. (2016), Enhanced O₂⁺ loss at Mars due to an ambipolar electric field from
549 electron heating, *J. Geophys. Res. Space Physics*, 121, 4668–4678,
550 doi:[10.1002/2016JA022349](https://doi.org/10.1002/2016JA022349).

551 Flynn, C. L., Vogt, M. F., Withers, P., Andersson, L., England, S., & Liu, G. (2017). MAVEN
552 observations of the effects of crustal magnetic fields on electron density and temperature
553 in the Martian dayside ionosphere. *Geophysical Research: Letters*, 44, 10,812–
554 10,821. <https://doi.org/10.1002/2017GL075367>

555 Fowler, C. M., Andersson, L., Ergun, R. E., Morooka, M., Delory, G., Andrews, D. J., Lillis, R.
556 J., McEnulty, T., Weber, T. D., Chamandy, T. M., et al. (2015), The first in situ electron
557 temperature and density measurements of the Martian nightside ionosphere, *Geophys.*
558 *Res. Lett.*, 42, 8854–8861, doi:[10.1002/2015GL065267](https://doi.org/10.1002/2015GL065267).

559 Fowler, Christopher, New insights into the structure and energetics of the Martian ionosphere
560 (2016). Astrophysical and Planetary Sciences Graduate Theses and Dissertations. 50.
561 https://scholar.colorado.edu/astr_gradetds/50

562 Fowler, C. M., et al. (2018a), Correlations between enhanced electron temperatures and
563 electric field wave power in the Martian ionosphere, *Geophys. Res. Lett.*, 45, 493–501,
564 doi: 10.1002/2017GL073387.

565 Fowler, C. M., Andersson, L., Ergun, R. E., Harada, Y., Hara, T., Collinson, G., et al.
566 (2018b). MAVEN observations of solar wind-driven magnetosonic waves heating the
567 Martian dayside ionosphere. *Journal of Geophysical Research: Space Physics*, 123, 4129–
568 4149. <https://doi.org/10.1029/2018JA025208>

569 Fox, J. L. (1993), The production and escape of nitrogen atoms on Mars, *J. Geophys. Res.*, 98,
570 3297–3310, doi:10.1029/92JE02289.

571 Fox, J. L., and A. B. Hac (2009), Photochemical escape of oxygen from Mars: A comparison of
572 the exobase approximation to a Monte Carlo method, *Icarus*, 204 (2), 527–544.

573 Gröller, H., Montmessin, F., Yelle, R. V., Lefèvre, F., Forget, F., Schneider, N. M., et al. (2018).
574 MAVEN/IUVS stellar occultation measurements of Mars atmospheric structure and
575 composition. *Journal of Geophysical Research: Planets*, 123, 1449–1483.
576 <https://doi.org/10.1029/2017JE005466>

577 Jakosky, B.M., Lin, R.P., Grebowsky, J.M. et al. *Space Sci Rev* (2015) 195: 3.
578 <https://doi.org/10.1007/s11214-015-0139-x>

579 Lillis, R. J., D. A. Brain, S. W. Bougher, F. Leblanc, J. G. Luhmann, B. M. Jakosky, R. Modolo, J.
580 Fox, J. Deighan, X. Fang, et al. (2015), Characterizing atmospheric escape from Mars today
581 and through time, with MAVEN, *Space Science Reviews*, 195 (1–4).

582 Lillis, R. J., et al. (2017), Photochemical escape of oxygen from Mars: First results from MAVEN
583 in situ data, *J. Geophys. Res. Space Physics*, 122, 3815–3836, doi:[10.1002/2016JA023525](https://doi.org/10.1002/2016JA023525).

584 Peterson, W. K., et al. (2016), Photoelectrons and solar ionizing radiation at Mars:
585 Predictions versus MAVEN observations, *J. Geophys. Res. Space Physics*, 121, 8859–
586 8870, doi:10.1002/2016JA022677

587 Peterson, W. K., Fowler, C. M., Andersson, L. A., Thiemann, E. M. B., Jain, S. K., Mayyasi, M., et
588 al. (2018). Martian electron temperatures in the subsolar region: MAVEN observations

589 compared to a one-dimensional model. *Journal of Geophysical Research: Space Physics*,
590 123. <https://doi.org/10.1029/2018JA025406>.

591 [Rees, M.H. \(1989\), *Physics and chemistry of the upper atmosphere, Cambridge Atmospheric*
592 *and Space Science Series, Cambridge University Press, ISBN: 9780521368483*](#)

593 McFadden, J.P., et al. (2015), MAVEN SupraThermal and Thermal Ion Composition (STATIC)
594 Instrument, *Space Sci. Rev.*, 195, 199, doi: 10.1007/s11214-015-0175-6.

595 Mahaffy, P., et al. (2015), The Neutral Gas and Ion Mass Spectrometer on the Mars Atmosphere
596 and Volatile Evolution Mission, *Space Sci. Rev.*, 195, 49, doi:10.1007/s11214-014-0091-1.

597 Matta, Majd et al., (2014), Numerical simulations of ion and electron temperatures in the
598 ionosphere of Mars: Multiple ions and diurnal variations, *Icarus*, 227, 78,
599 doi:10.1016/j.icarus_2013.09/006.

600 Mendillo, M., Narvaez, C., Vogt, M. F., Mayyasi, M., Forbes, J., Galand, M., ... Andersson,
601 L. (2017). Sources of ionospheric variability at Mars. *Journal of Geophysical Research: Space*
602 *Physics*, 122, 9670– 9684. <https://doi.org/10.1002/2017JA024366>

603 Mitchell, D.L. C. Mazell, J.-A. Sauvaud, J.-J. Thocaven, J. Rouzaud, A. Fedorov, P. Rouger,
604 D. Toublanc, E. Taylor, D. Gordon, M. Robinson, S. Heavner, P. Turin, M. Diaz-
605 Aguado, D. W. Curtis, R. P. Lin, and B. M. Jakosky (2016), The MAVEN solar wind electron
606 analyzer (SWEA), *Space Sci. Rev.* xx, 34, doi: 10.1007/s11214-015-0232-1.

607 Morrison, M. A., and A. E. Greene (1978), Electron cooling by excitation of carbon dioxide, *J.*
608 *Geophys. Res.*, 83(A3), 1172–1174, doi:[10.1029/JA083iA03p01172](https://doi.org/10.1029/JA083iA03p01172).

609 Nagy, A.F, J.P. Doering, W.K. Peterson, M.R. Torr, and P.M. Banks (1977), Comparison Between
610 Calculated and Measured Photoelectron Fluxes from Atmosphere Explorer C and E, *J.*
611 *Geophys. Res.* 82, 5099, doi: [10.1029/JA082i032p05099](https://doi.org/10.1029/JA082i032p05099)

612 Sakai, S., et al. (2016), Electron energetics in the Martian dayside ionosphere: Model
613 comparisons with MAVEN data, *J. Geophys. Res. Space Physics*, 121, 7049–7066,
614 doi:10.1002/2016JA022782.

615 Sakai, S., Cravens, T. E., Andersson, L., Fowler, C. M., Mitchell, D. L., Mazelle, C., et al. (2019).
616 Low electron temperatures observed at Mars by MAVEN on dayside crustal magnetic field
617 lines. *Journal of Geophysical Research: Space Physics*, 124. [https://](https://doi.org/10.1029/2019JA026961)
618 doi.org/10.1029/2019JA026961

619 Schunk, Robert, and Andrew Nagy (2009), *Ionospheres: Physics, Plasma Physics, and Chemistry*,
620 Cambridge University Press.

621 Shinagawa, H., and T. E. Cravens (1989), A one-dimensional multi-species
622 magnetohydrodynamic model of the dayside ionosphere of Mars, *J. Geophys. Res.*, 94,
623 6506, doi:10.1029/JA094iA06p06506.

624 Stone, S. W., Yelle, R. V., Benna, M., Elrod, M. K., & Mahaffy, P. R. (2018). Thermal structure of
625 the Martian upper atmosphere from MAVEN NGIMS. *Journal of Geophysical Research:*
626 *Planets*, 123, 2842–2867. <https://doi.org/10.1029/2018JE005559>

627 Thiemann, E. M. B., P. C. Chamberlin, F. G. Eparvier, B. Templeman, T. N. Woods, S. W.
628 Bougher, B. M. Jakosky (2017), The MAVEN EUVM model of solar spectral irradiance
629 variability at Mars: Algorithms and results, *J. Geophys. Res. Space Physics*, 122, 2748–2767,
630 doi:[10.1002/2016JA023512](https://doi.org/10.1002/2016JA023512).

631 Thiemann, E. M. B., Andersson, L., Lillis, R., Withers, P., Xu, S., Elrod, M., et al. (2018). The Mars
632 topside ionosphere response to the X8.2 solar flare of 10 September 2017. *Geophysical*
633 *Research Letters*, 45,8005– 8013. <https://doi.org/10.1029/2018GL077730>
634 Withers, P., K. Fallows, and M. Matta (2014), Predictions of electron temperatures in the Mars
635 ionosphere and their effects on electron densities, *Geophys. Res. Lett.*, 41, 2681–2686,
636 doi:10.1002/2014GL059683.
637 Xu, S., Thiemann, E., Mitchell, D., Eparvier, F., Pawlowski, D., Benna, M., al.,
638 et (2018). Observations and modeling of the Mars low-altitude ionospheric response to
639 the 10 September 2017 X-Class solar flare. *Geophysical Research Letters*, 45, 7382–
640 7390. <https://doi.org/10.1029/2018GL078524>.

Figure 1.

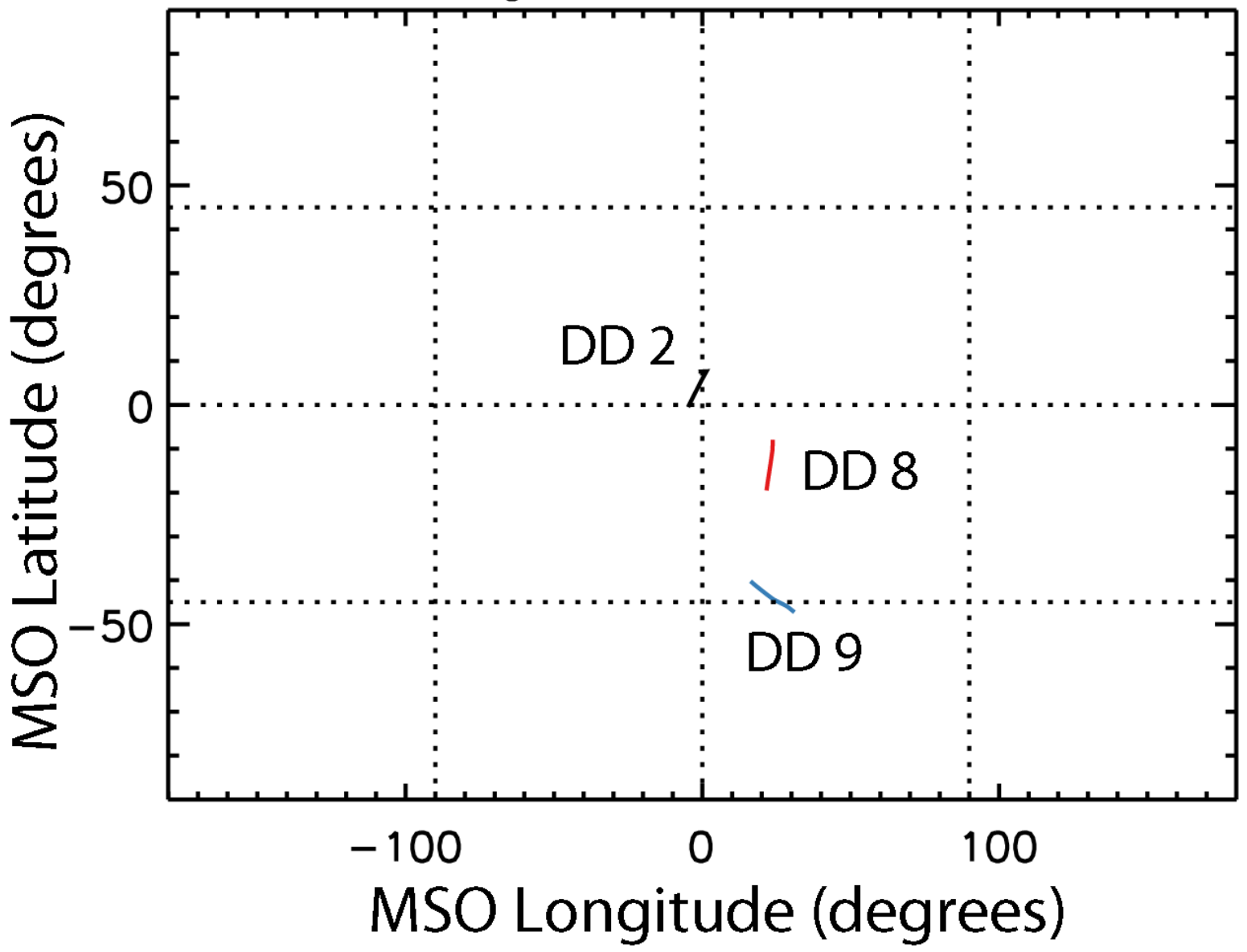


Figure 2.

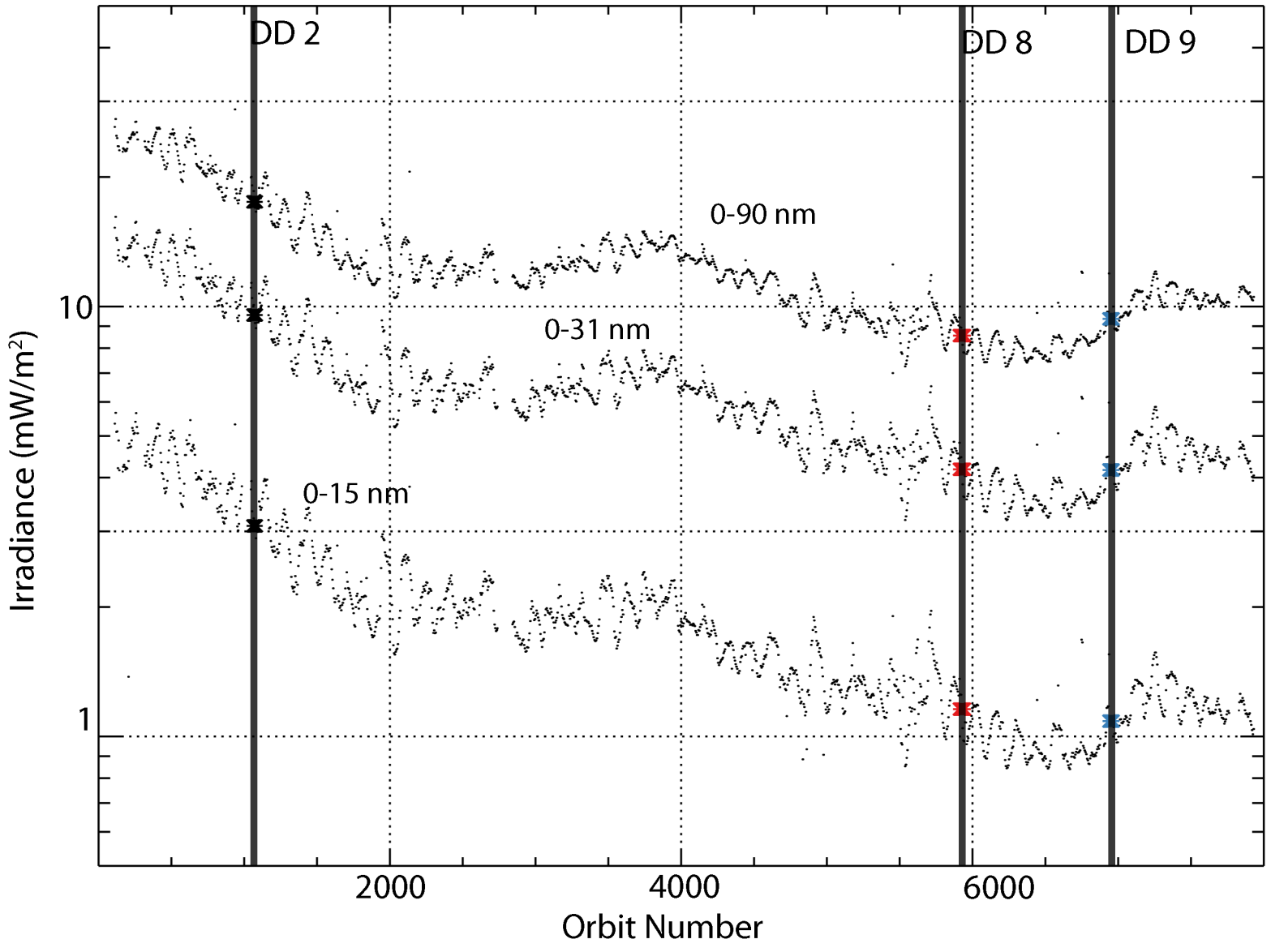


Figure 3.

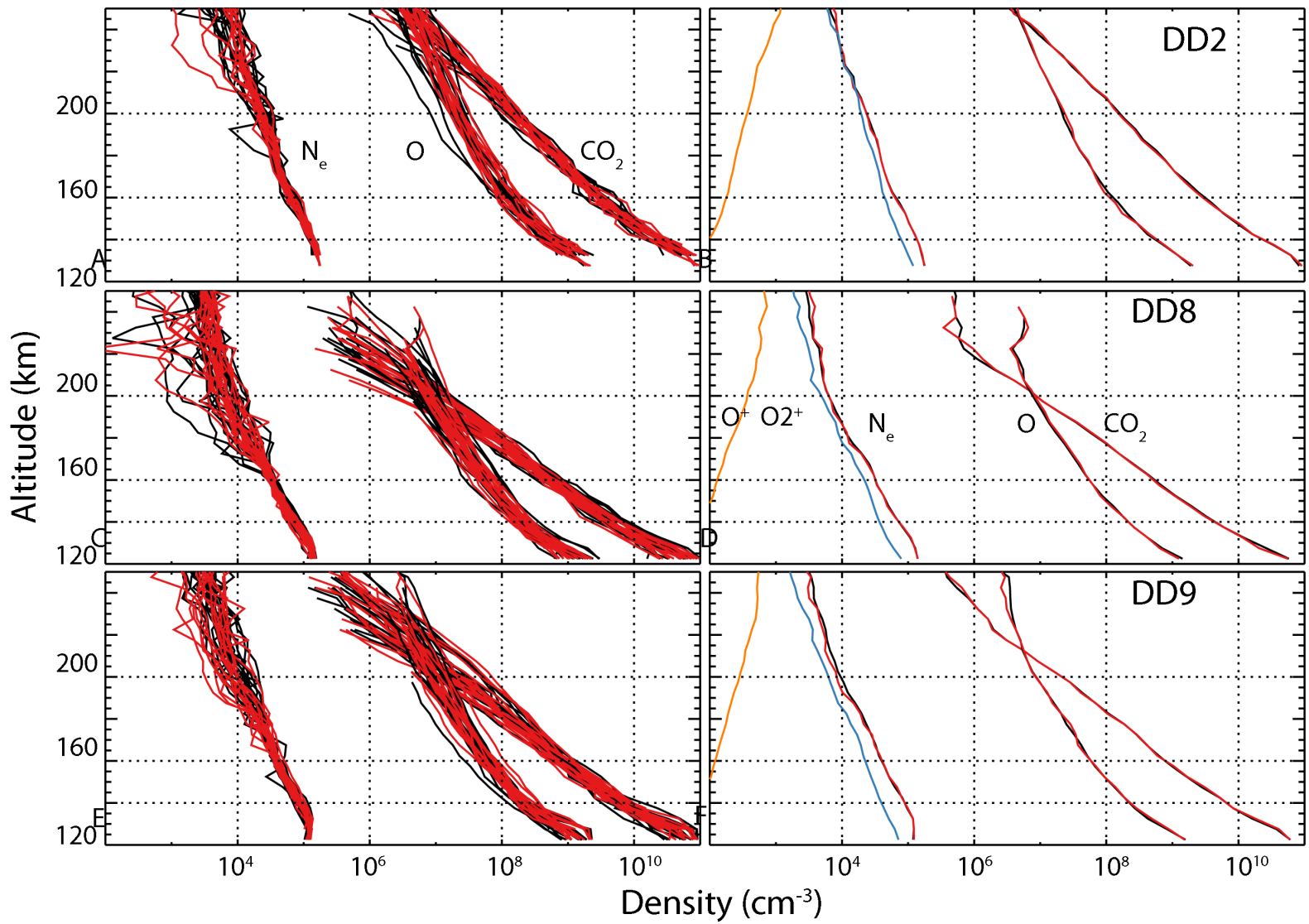


Figure 4.

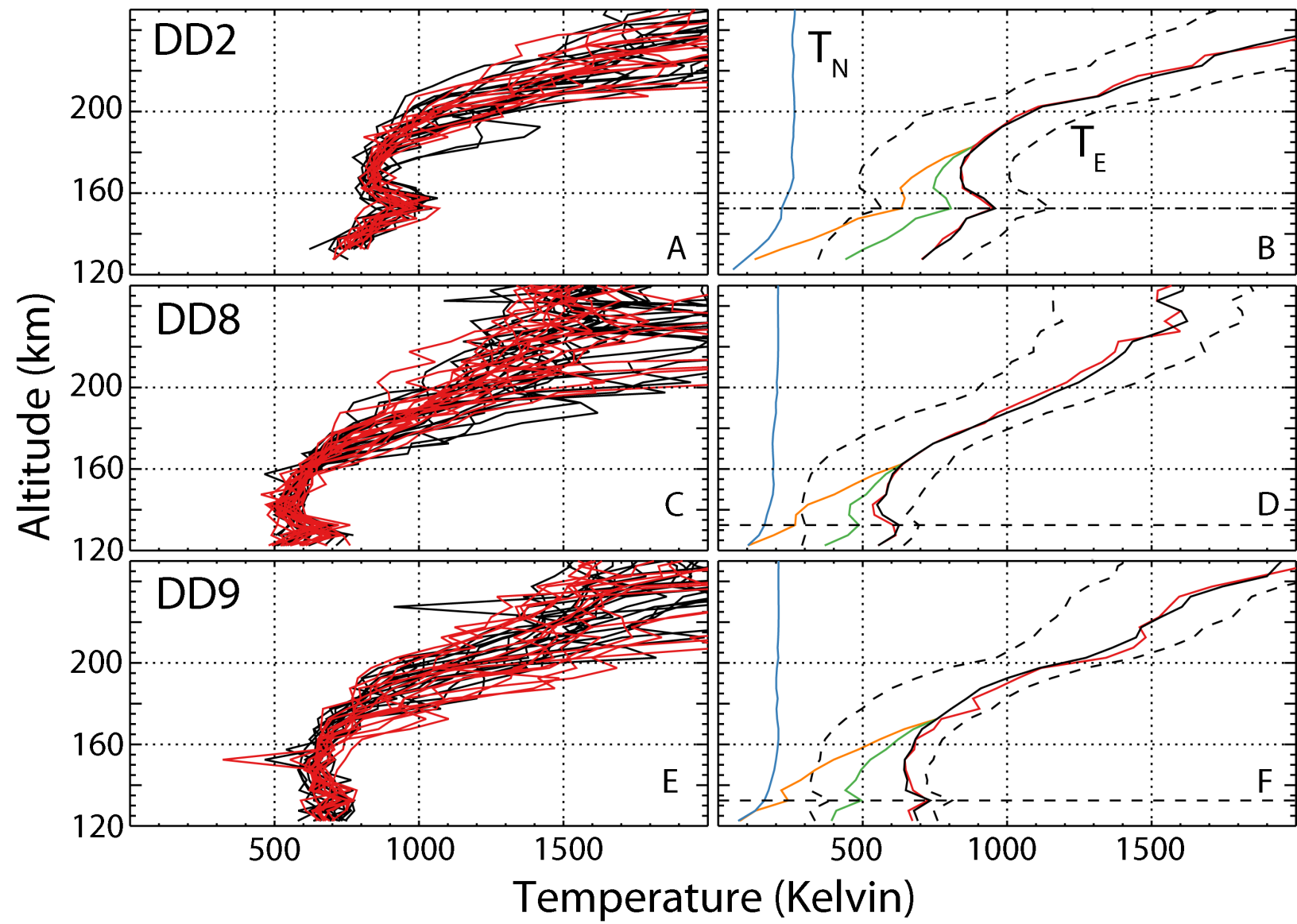


Figure 5.

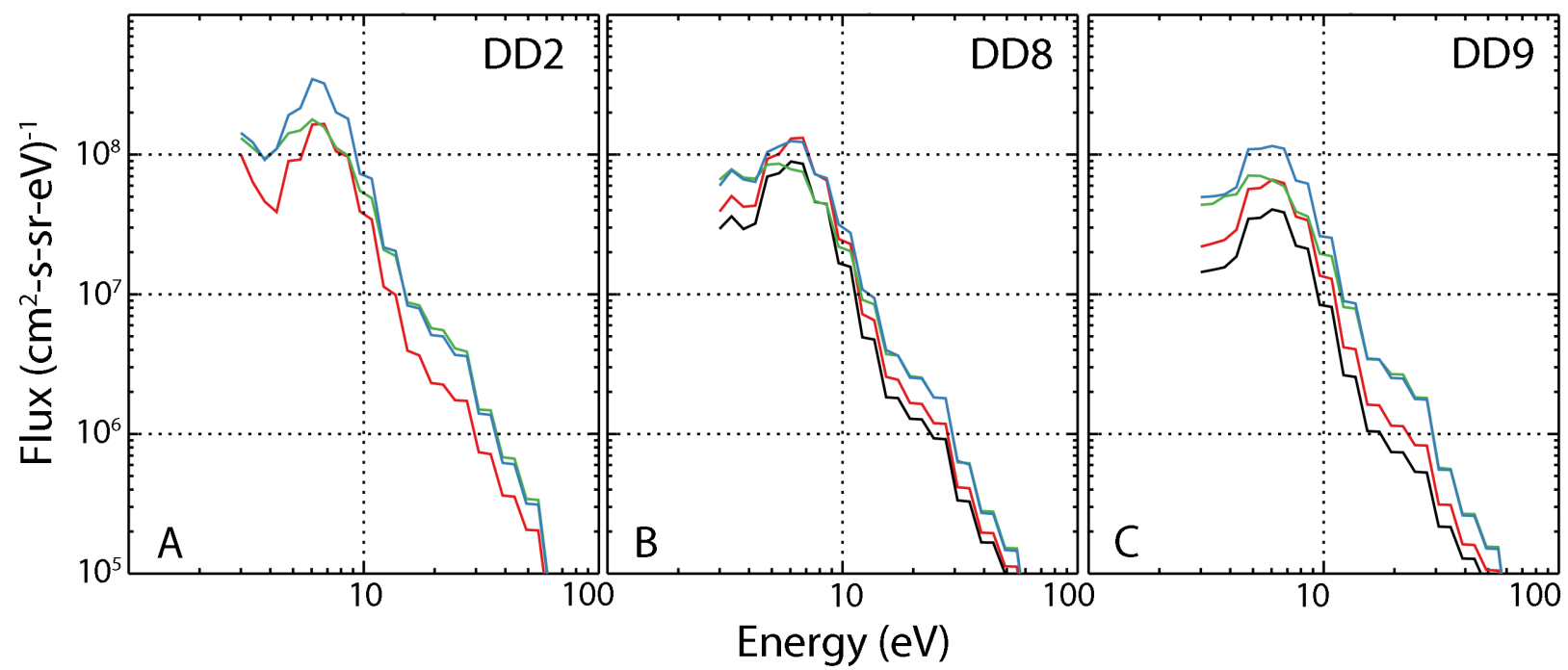


Figure 6.

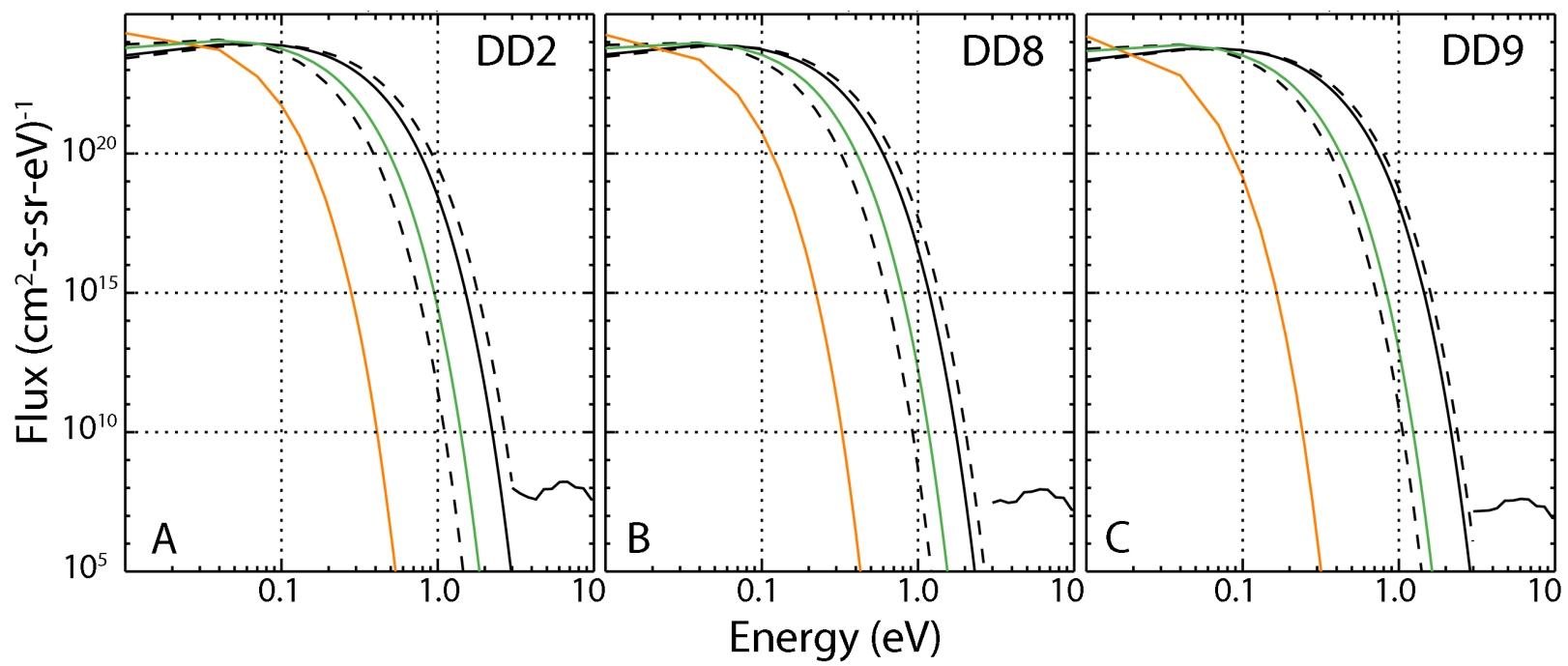


Figure 7.

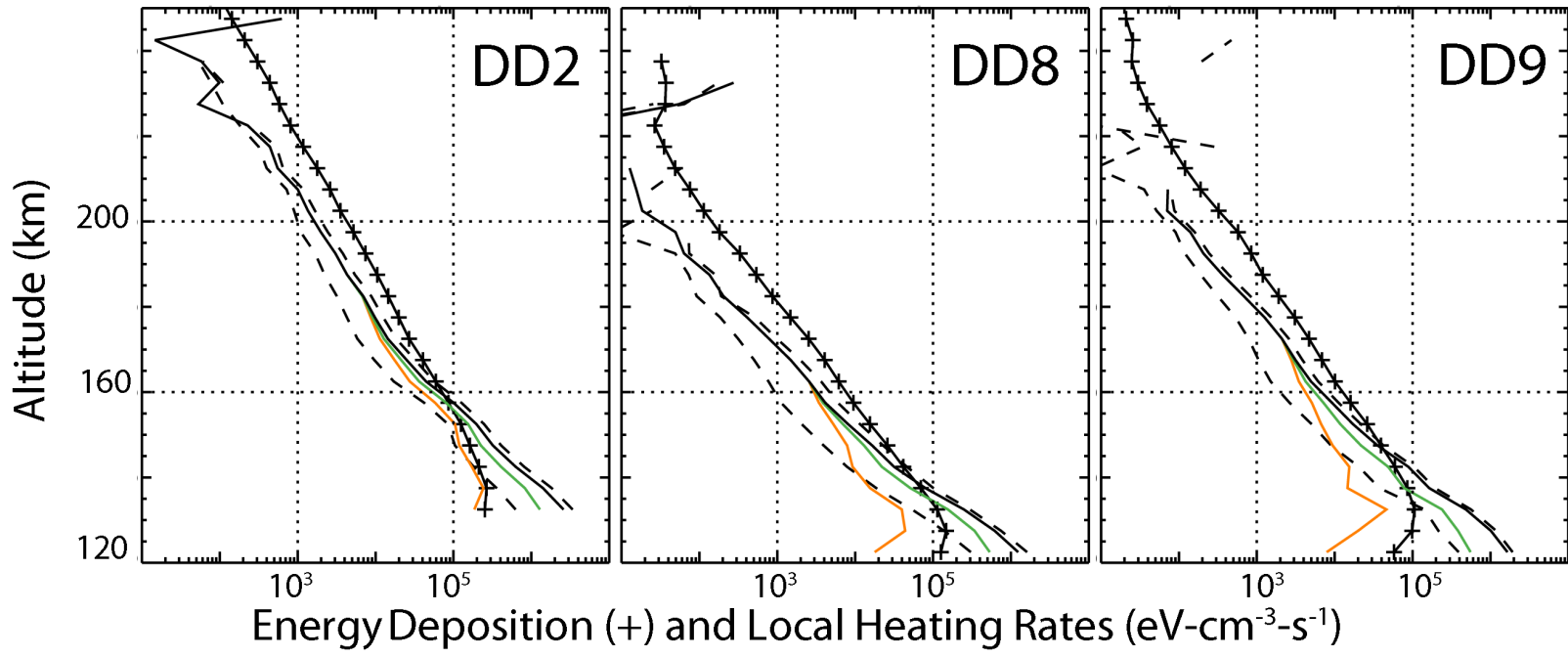


Figure 8.

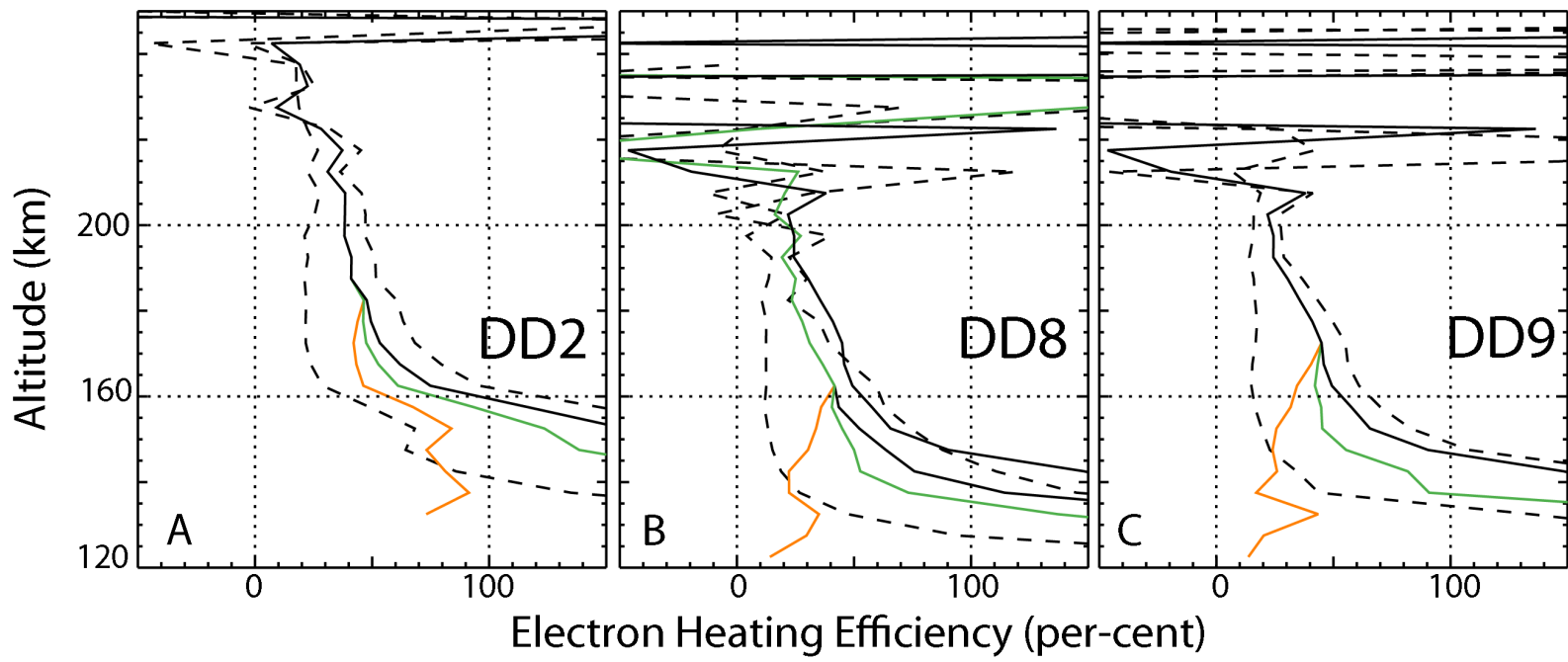


Figure 9.

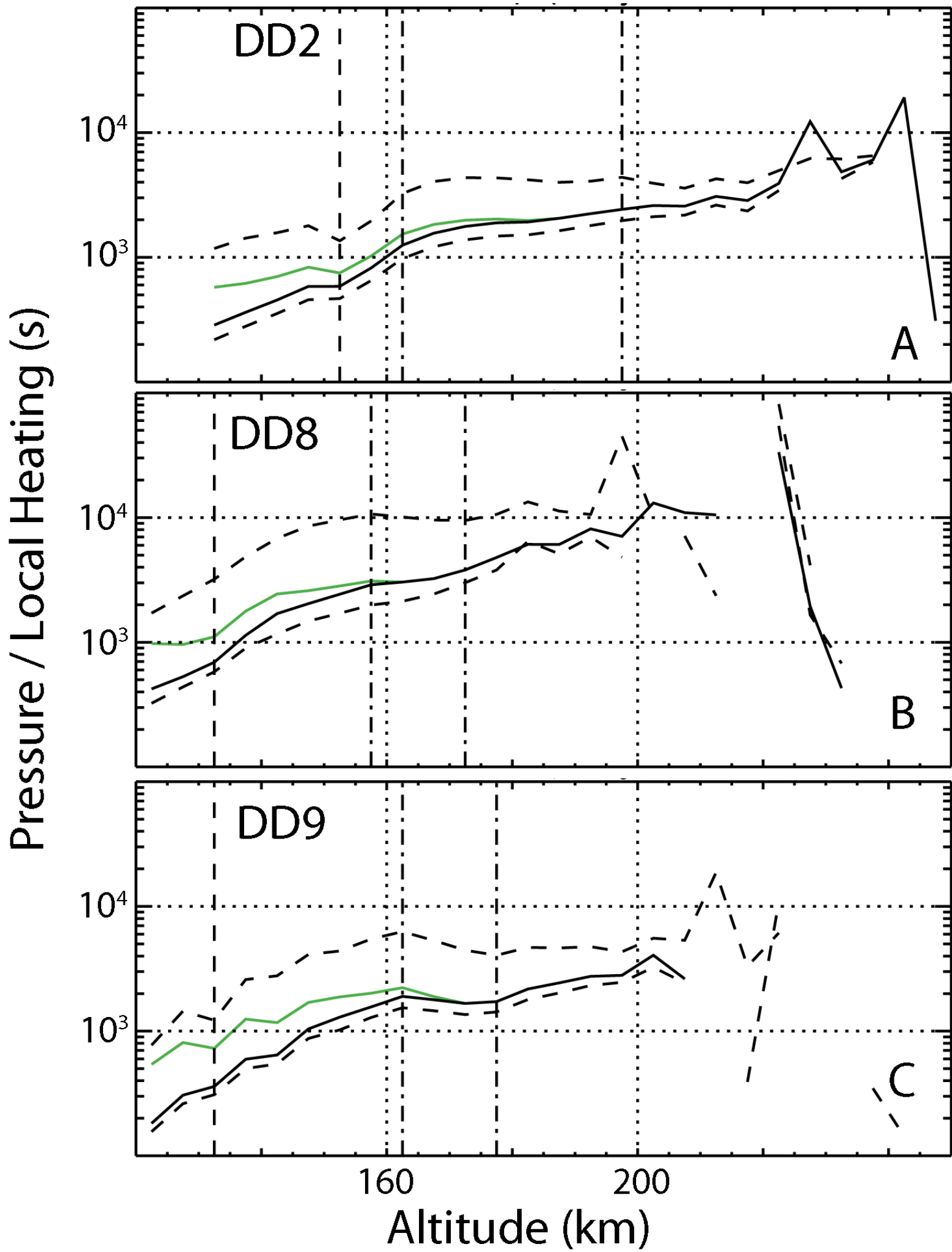


Figure 10.

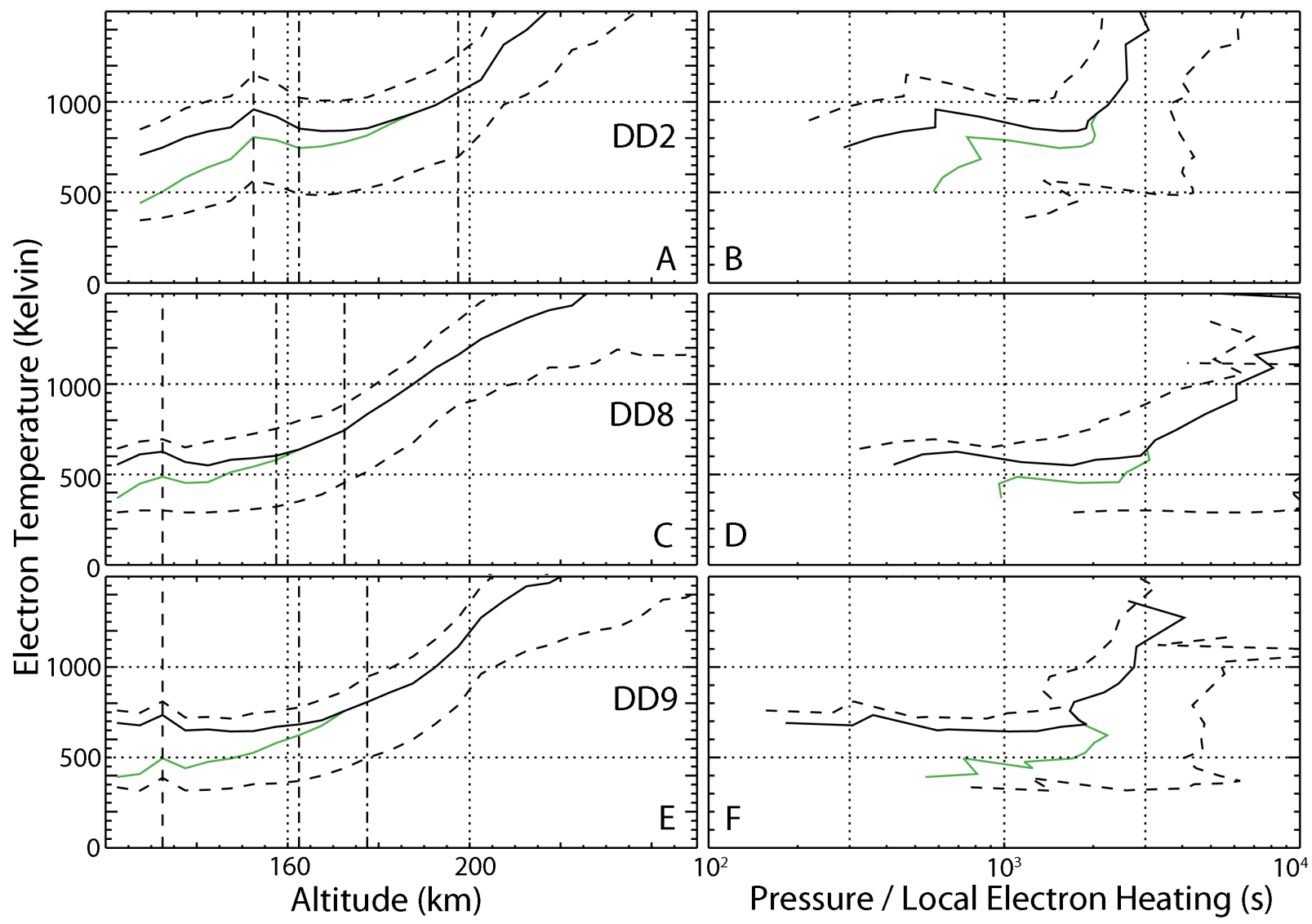


Figure 11.

